July 2018

High Strain Rate Dynamic Response of Aluminum 6061 Micro Particles at Elevated Temperatures and Varying Oxide Thicknesses of Substrate Surface

Carmine Taglienti

HIGH-STRAIN-RATE DYNAMIC RESPONSE OF ALUMINUM 6061 MICROPARTICLES AT ELEVATED TEMPERATURES AND VARYING OXIDE THICKNESSES OF SUBSTRATE SURFACE

A Thesis Presented

by

CARMINE S. TAGLIENTI

Submitted to the Graduate School of the
University of Massachusetts Amherst in partial fulfillment
of the requirements for the degree of

MASTER OF SCIENCE IN
MECHANICAL ENGINEERING

May 2018

Mechanical and Industrial Engineering

HIGH-STRAIN-RATE DYNAMIC RESPONSE OF ALUMINUM 6061 MICROPARTICLES AT ELEVATED TEMPERATURES AND VARYING OXIDE THICKNESSES OF SUBSTRATE SURFACE

A Thesis Presented

by

CARMINE S. TAGLIENTI

Approved as to style and content by:

_____
Professor Jae-Hwang Lee, Chair

_____
Professor David Schmidt, Member

_____
Professor, Jonathan Rothstein, Member

_____
Sundar Krishnamurty, Department Head
Program Director
Mechanical and Industrial Engineering

ACKNOWLEDGEMENTS

Funding was provided by the Army Research laboratory (Materials Manufacturing Technology Branch: RDRL-WMM-D) and by the U.S. Army Research Office, under contract W911NF-15-2-0024, titled “Intelligent Processing of Materials by Design”.

ABSTRACT

HIGH-STRAIN-RATE DYNAMIC RESPONSE OF ALUMINUM 6061 MICROPARTICLES AT ELEVATED TEMPERATURES AND VARYING OXIDE THICKNESSES OF SUBSTRATE SURFACE

MAY 2018

CARMINE S. TAGLIENTI,

B.S., UNIVERSITY OF MASSACHUSETTS AMHERST

M.S., UNIVERSITY OF MASSACHUSETTS AMHERST

Directed by: Professor Jae-Hwang Lee

Cold spray is a unique additive manufacturing process, where a large number of ductile metal micro particles are deposited to create new surface coatings or free-standing structures. Metallic particles are accelerated through a gas stream, reaching velocities of over 1 km/s. Accelerated particles experience a high-strain-rate microscopic ballistic collisions against a target substrate. Large amounts of kinetic energy results in extreme plastic deformation of the particles and substrate. Though the cold spray process has been in use for decades, the extreme material science behind the deformation of particles has not been well understood due to experimental difficulties arising from the succinct spatial (10 μm) and temporal scales (10 ns).

In this study, using a recently developed micro-ballistic method, the advanced laser induced projectile impact test (α-LIPIT), the dynamic behavior of micro-particles during the collision is precisely defined. We observe single aluminum 6061 alloy particles, approximately 20 μm in diameter, impact and rebound off of a rigid target surface over a broad range of impact speeds, temperatures, and substrate oxide film thicknesses. Through observation of the collisions, we extract characteristic information

of the dynamic response of particles as well as the relationship with various parameters (e.g. surrounding temperature, particle diameter, oxide thickness, and impact velocity). By impacting a polished aluminum 6061 alloy substrate we are able to mimic the collision events that occur during cold spray deposition. The connection between the temperature increase and the oxide thickness plays a role in theorizing the cause of unexpected phenomena, such as increased rebound energies at higher temperatures. Highly-controlled single particle impacts results, are provided to calibrate and improve computational simulations as well. This, in turn, can provide insight into the underlying material science behind the cold spray process.

TABLE OF CONTENTS

Page

LIST OF TABLES

Table Page

LIST OF FIGURES

Figure Page

CHAPTER 1

INTRODUCTION AND MOTIVATION

Cold Spray Process

Additive manufacturing techniques have been an area of great interest to industry and researchers alike. The use of metals in additive manufacturing has proven to be challenging since only a few methods are able to substantiate results, such as selective laser or electron beam melting.[1] The solid-state deposition technique, titled cold spray (CS), utilizes supersonic impacts of micro particles (10-100 μm in diameter) to build up coatings and/or free-standing structures. The high velocity impact results in severe plastic deformation and bonding of the particle to the substrate and/or previously deposited particles. An advantage of CS is that deposition and bonding is achieved over short interaction times at temperatures lower than materials' melting point. At comparatively low temperatures, CS is able to avoid the consequences of high temperature material modification including oxidation, residual thermal stresses, and unfavorable structural changes in powder material caused by melting and re-solidification. Ang *et al*. compared various thermal spray techniques in terms of the particle impact velocity and process temperature. **Figure 1** shows that the temperature of CS is far less than other thermal spray techniques, while still achieving the high velocities necessary for particle deposition.[1]

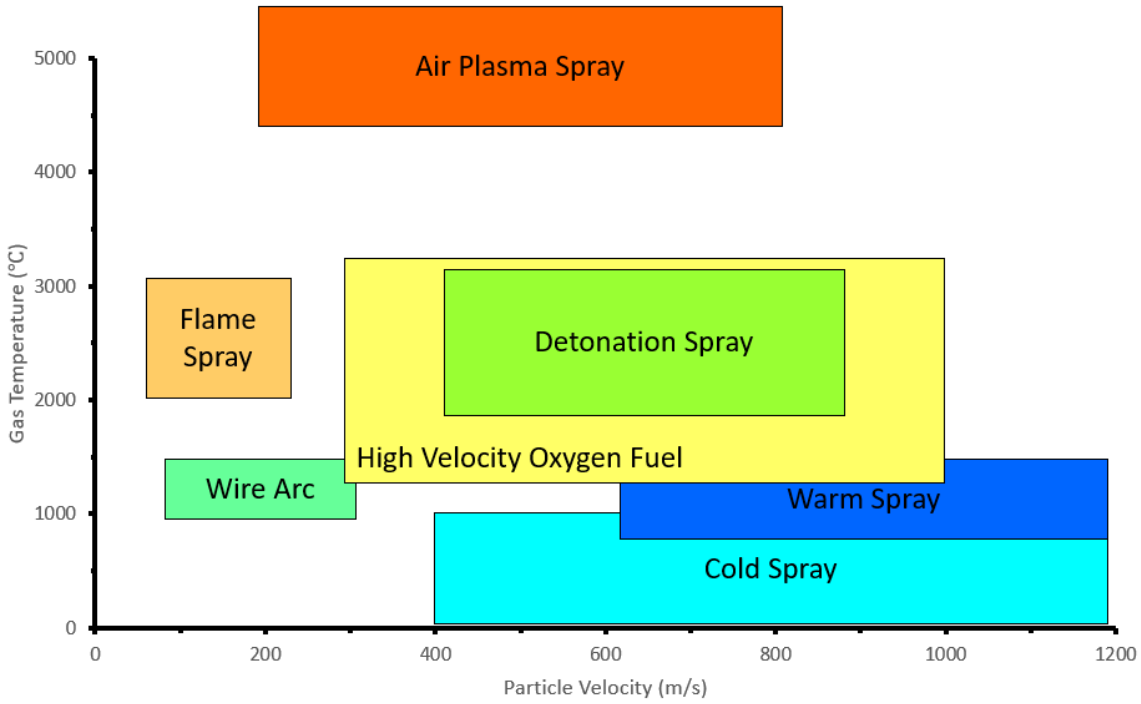

Figure 1: Classification of various thermal spray processes as the impact velocity relates to gas propellant temperature.[1]

As a result of the high impact speeds, the particles-substrates interaction time is short, on the order of 10 ns. The low process temperature also allows for the structures within the materials to be preserved without significant recrystallization. Additionally, it has been discovered by Thevamaran *et al*. that the lack of recrystallization present in this process has the potential to yield nano-scale grain gradients throughout the resulting structure, which can prove to be advantageous when precise control over the bulk properties is desired.[2-4] CS is beneficial when compared to other additive manufacturing techniques and thermal spray processes by leveraging the advantage produced by the large plastic deformation. As opposed to thermal energy, which would cause significant changes in the original material, CS used kinetic energy to achieve particle deposition[5].

CS technology has many promising aspects; it is used to create thick coatings on metal or even ceramic surfaces leading to new surface characteristics of the material. It

has even been shown that both metal and metal-coated ceramic particles are able to be accelerated and bonded to various surfaces in order to create unique coatings. CS is also used to create free-standing structures in an additive manner. Lastly, CS has the capacity to repair damaged structures and surfaces rapidly, resulting in a restored or filled part with comparable properties to the original.[5] CS was first invented over three decades ago at the Institute of Theoretical and Applied Mechanics in Novosibirsk, Russia.[6,7] Serious developments in CS were not seen until the 1990's.[8] This method has been growing in popularity not only in industry, but also in the academic community, with a large number of publications being produced in the last two decades; in order to understand the physical phenomena occurring in this process.[5,9-11] The understanding of this topic requires the incorporation of many fields of research, including fluid dynamics, solid mechanics, and material science. Although CS has been leveraged for decades, the governing material science behind how this process works is not fully established.

In this additive method, various ductile metals are deposited on a substrate well below their melting temperature. **Figure 2** shows a sketch of a common CS apparatus.

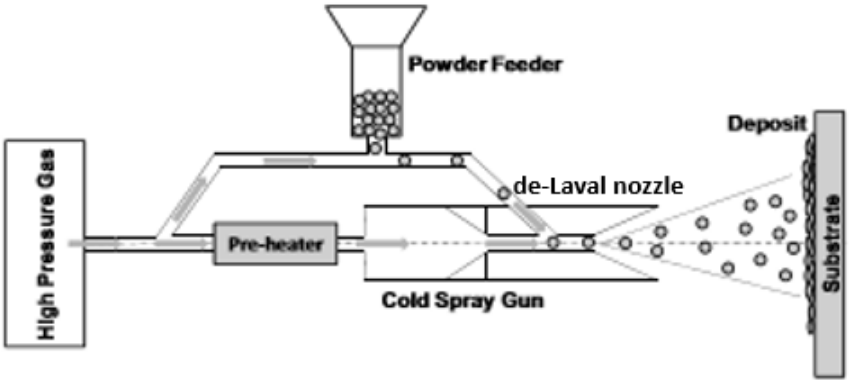

Figure 2: Schematics of the main components of a typical cold-spray apparatus.

Powders, containing micro particles 10-100 μm in diameter depending on the material used, are sprayed through a converging-diverging de Laval nozzle at high speeds using a pressurized carrier gas, usually nitrogen or sometimes helium, at a rate of 10^5-10^7 particles per second. The temperature of the electrically heated gas can reach up to 1,000℃ depending on the desired particle speed. However, the temperature of the particles on impact range from 20-800℃, depending on many factors such as the gas, nozzle design and heat capacity of the material.[12] Particles then impact the selected surface or substrate, applying the desired coating or structure. At these high deposition rates and velocities, it is challenging to observe individual particle collisions. Obviously, there is a large amount of variation between the impact parameters of each individual particle.

It has been well studied that if the impact velocity exceeds a specific critical value, the energy will be enough to induce severe enough plastic deformation resulting in the bonding of the particle to the target, which can either be a fresh surface or particles that had previously been deposited. This critical velocity is related to successful bonding and depends most significantly on the thermomechanical properties of the particle and substrate materials, but is also a function of particle size, initial temperature and melting temperature.[13-16] It is understood that if the energy required for bonding exceeds the elastic energy stored in the particle upon deformation on impact the particle can bond to the surface. Otherwise the particle is reflected off the surface.[17] The visco-plastic deformation experienced leads to two key phenomena of CS; sequential compaction of deposited layers into a solid and metallurgical bonding between the particles and substrate over a large fraction that interfaces. Both are required to have a dense and

strong resultant structure. If the powder is not efficiently compacted by subsequent impacts, the resultant will be highly porous. Furthermore, if there is poor bonding at the particle-substrate and particle-particle interfaces, the resultant structure will have low strength.[18] These factors are why reaching and exceeding the critical velocity is essential to CS.

The two factors required for effective CS structures discussed are the result of severe deformation of the accelerated particle. In order to improve CS deposition, the deformation process must be understood. Various hypotheses have been introduced as to the fundamental material science behind the bonding mechanisms such as material interlocking by interface instability, cohesive bonding, adiabatic shear instabilities, and local melting.[8, 19-21] Material interlocking is achieved through the compaction of subsequent layers of material. This happens when the particle-substrate collision creates a crater that physically holds the particle in place. Hussain *et al.* states that in most cases, mechanical interlocking can account from the majority of bond strength when there if good deposition and low porosity.[22] Even if earlier particle impacts do not have good adhesion to the impact surface, following impacts will improve that adhesion through repeated impacts, creating a stronger bulk material.[22] Another prevailing hypothesis is that extreme plastic deformation disrupts the thin surface oxide films surrounding metals exposing chemically active material; under high local pressure, metallurgical bonding is achieved in these exposed interfacial areas (**Figure 3)**.[23]

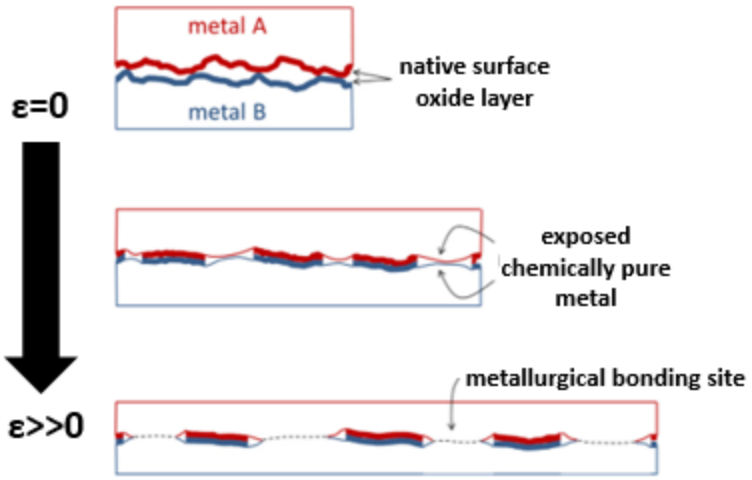

Figure 3: Schematics of interfacial area between two metal surfaces in a high-strain-rate collision. Extreme plastic deformation results in cracking of the surface layer and exposure of pure metal surfaces as the strain increases.[23]

Metallurgical bonding is a result of atomic diffusion between metals, which provides stronger bonding than mechanical interlocking.[24] This bonding process is similar to the events present in explosive welding and shock wave powder compaction.[25, 26] Adiabatic shear instabilities are characteristically associated with high-strain-rate (HSR) deformations and are cause of the extreme plastic deformation observed at the collision interface; it is predicted that they lead to metallurgical bonding. Adiabatic shear instabilities are so critical to creating metallurgical bonds that they may be considered a requirement for bonding, and consequently are assumed to be an indicator of bonding.[21] Under adiabatic conditions, as opposed to isothermal, the plastic strain energy is dissipated. As heat increases during deformation, the temperature rise causes the material to soften. It is easier for softened material to deform and produce heat. As a result, the rate of strain hardening decreases and the flow stress reaches a maximum then decreases with increasing plastic strain. In a real non-uniform material however, variations in stress, strain, temperature, and microstructure are present throughout. These variations cause

shearing, heating and softening to become highly localized, causing the flow stress to drop rapidly at a critical strain (**Figure 4)**. Beyond this point, local strain at the shear band increases while the overall strain remains almost constant until rupture.[27-29]

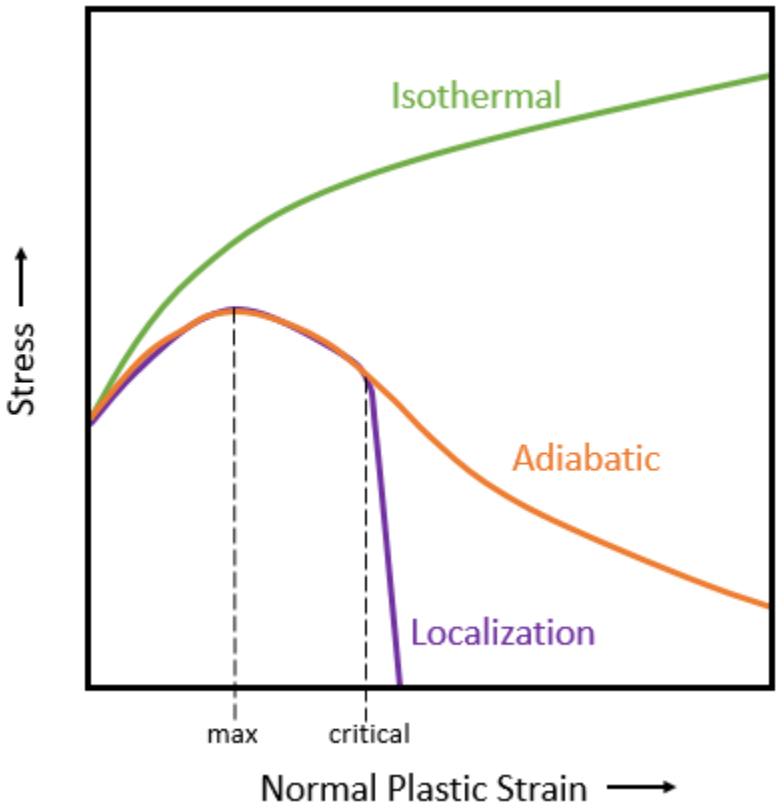

Figure 4: Plot of stress-strain variation for a typical bulk metallic material during a torsion experiment. Isothermal, adiabatic, and localization curves are shown.[28]

This concentration of stress and temperature around the interface region results in the formation of a jet, which is widely observed in both experimentation and simulation.[15, 30, 31] At the interface region, adiabatic thermal softening is dominant over work hardening and the metals behave as viscous materials at this highly localized area. Due to the pressure, the material is extruded from the interface forming the metal jet at the rim.[21, 29] A simple sketch of the jet formation during a typical ductile metal collision above the critical velocity is presented in **Figure 5a**.

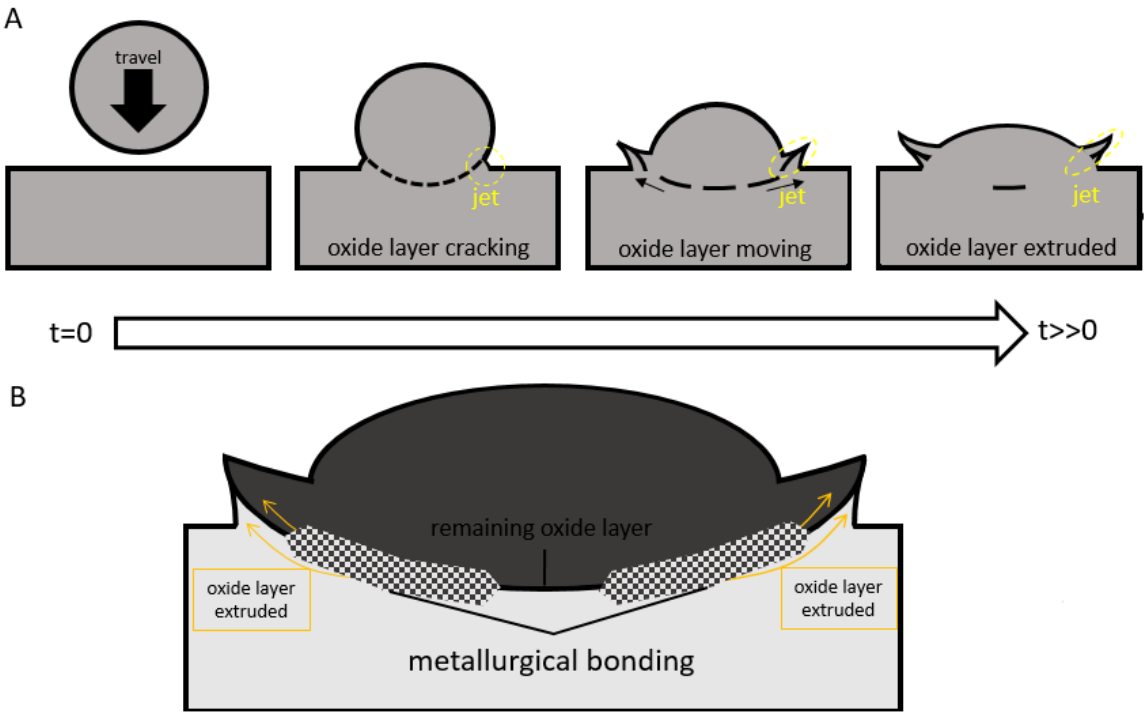

Figure 5: A) Sequential sketch of the formation of a material jet for a typical ductile metal micro-particle impacting a like-substrate over the critical velocity. B) Sketch of the postmortem bonded particle, highlighting the bonding at the rim, where oxide was removed and lack thereof in the center, where oxide remains as a barrier.

Another observation is that the strongest bonding occurs at the edges of the interfacial region. It has been observed that there is more interaction of the material in these locations due to the displacement of the oxide film, which forms the jet, allowing for pure material interaction (**Figure 5b**).[32] In this viscous region, there are vortices formed of interacting material, which result in not only metallurgical bonding but also interlocking of particle and substrate material, further increasing the strength of the bonding in this critical region of the interface.[33] These concepts are typical for crystalline metals and alloys with work-hardening and thermally activated deformation behaviors. Through numerical analysis, Hussain *et al.* observed highly localized temperature rises large enough to induce localized melting which would influence bonding.[22, 34] Studies have

evaluated the role of interfacial melting in bonding and reported that adiabatic shear instabilities lead to a thin layer of melting at the interface for some material combinations.[22, 34-37] It is currently argued whether localized melting at the interface is required for bonding; however, mechanical interlocking and metallurgical bonding caused by the presence of adiabatic shear instabilities are commonly perceived as the dominant mechanisms responsible for bonding during CS.

The impact of a CS particle onto its substrate can be broken down into 4 distinct phase by Zhoe *et al*. The first phase is transient loading; this is when the particle comes into contact with the substrate and the high kinetic energy begins to put extreme pressures on the initial contact point. The second phase is when the material starts to flow due to these high pressures. It is observed that the maximum pressure is much higher than the material's yield strength in most cases causing the material to deform. The high strains near the interface cause softening due to heating which further results in the shear instabilities, material vortices, metallurgical bonding and the jet formation. Kinetic energy is dispersed into heat through plastic strain which helps to reduce the pressure. In phase three, the lower pressure causes the plastic flow of material to stop and only elastic deformation to occur. Phase four is the elastic recovery of that stored energy. In this phase, the particle will either stay bonded or debond, depending on if the bonding cohesive energy resulting from interaction in phase two is greater than the stored elastic energy from phase three.[33] A plot of the pressure changes throughout these phases of the impact can be seen in **Appendix A**.

The bonding phenomenon has not been explicitly understood due to the non-linearity, non-equilibrium, and high-strain-rate response of the material. As discussed,

during the CS process large numbers of particles are accelerated, each having different impact parameters and different impact results, making the study of individual particles challenging. The particle interaction time upon impact is in the vicinity of 100 ns and the strain rates are on the order of 10^6-10^8 s^{-1}. These factors make observation of the impact through experimentation with a typical CS setup difficult. However, computational modeling can provide insight into these phenomenon, validation of hypotheses, or the discovery of a unique mechanisms. With computational simulations the deformation can be slowed and observed at any scale.

Simulation

In order to observe the material behavior of the particles during extreme deformation inherent to CS, computational analysis is required. Due to the small size and temporal scale, experimental observation of the collision event proves to be unfeasible. Thus, computational modeling has been dedicated to understanding the collision event critical to CS. With modeling, it is possible to view inside the micro-particles during the collision event step by step, track individual material points, and follow fluctuations in stresses and strains throughout the interaction. Computational simulation of single particle impacts is used to better understand the mechanics, however using this powerful tool, it is possible to extrapolate to bulk CS deposition as well. Over the years since the invention of CS, many researchers have performed simulations to study the extreme phenomenon by using a finite element (FE) method. Dykhuizen *et al*. simulated the collisions of copper micro-particles onto a stainless steel substrate and compared the calculated flattening ratios and crater depths with experimental findings.[36] Yokoyama *et al.* numerically studied the effects of an initial particle temperature on the behavior of

copper particles impacting copper and steel substrates.[37] Schmidt *et al.* and Bae *et al* investigated the main factors effecting bonding features, for several different particle material systems.[20, 23] Li *et al.* and Kumar *et al.* have studied the effects of oxide layers and other substrate surface conditions.[38, 39] Other variable CS parameters have also been investigated, including oblique impacts,[40] particle size,[41] substrate hardness,[42] and impact of multiple particle materials.[43, 44] These simulations are responsible for many of the discoveries discussed in the previous section, specifically the presences of adiabatic shear instabilities and the dramatic temperature rise at the interface.

Zhoe *et al.* in **Figure 6**, examines the plastic strain distribution in the particle and substrate during the impact. The simulation shows that the most severe deformation occurs at the interface. The plastic strain reaches more than 200% at the interface region, indicating the presence of heating and adiabatic shear instabilities in this thin interfacial layer.[33] These phenomena then result in the formation of the material jet also present in the simulation result, and the bonding mechanisms previously discussed. Simulations like this are the only way to understand the mechanisms taking place during the complex deformation process of CS impacts.

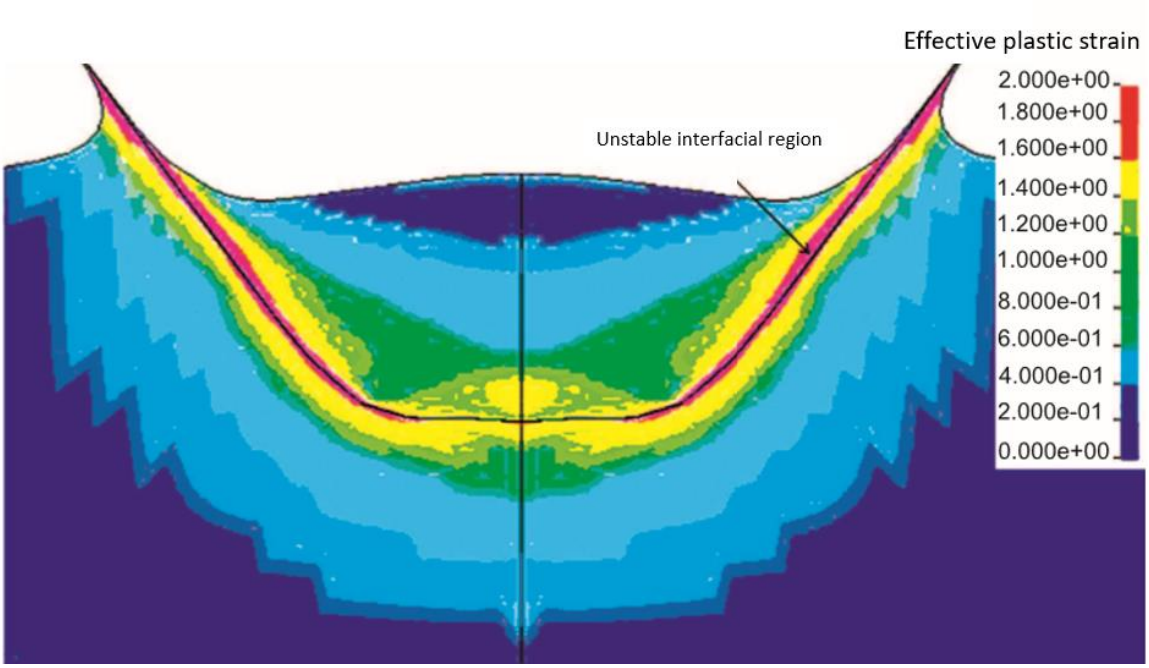

Figure 6: Simulation of the effective strain distribution of an impact of a particle and substrate of the same material. Strain will decrease further from the interface. Red indicates pure plastic strain or adiabatic instabilities. Blue and green indicates plastic-elastic strains. Purple represents purely elastic regions.[33]

Due to the extreme behavior of materials during the collision of a CS particle, the simulation results are very dependent on the modeling method used. A common modeling method uses a Lagrangian reference frame. In a Lagrangian reference frame, the mechanics of each material point are followed and the mesh moves with the deforming material points. This commonly leads to excessive mesh distortion during extreme material deformation. These large deformations can lead to the simulation failing; this can only be compensated for by having fewer, larger elements. However, larger elements do not provide the level of accuracy required for study of the micro particle collisions. Since the accuracy of the calculation is a function of the size of the mesh, using pure Largangian method is limited and unreliable.[45] In an Arbitrary Lagrangian Eulerian (ALE), material motion is independent from material inside the object. As a result, elements will not need to deform as much to follow these points. The

mesh is continuously updated without making changes to the mesh connections. The mesh updates first by forming a new mesh based on the current status, then the solution variables will be remapped to the new mesh. This method allows for a finer mesh. Although less dependent on mesh size, this method shows a decrease in plastic strain over time and the lack of a jet formation at the interface. The error is likely due to the remapping of the mesh.[46]

During CS, material bonding needs to be considered as well. Previously, bonding has been declared via observations of stress and temperature throughout the impact. Localized peaks in temperature and strain at the particle-substrate interface were observed in simulations and declared to be shear instabilities representative of bonding. The velocity which produced the changes in temperature and strain was considered to be the critical velocity.[21, 22, 28] In other simulations, the critical velocity was treated as the velocity that brought the temperature at the interface during impact above the melting temperature of the particle.[22, 34-37, 47] Thus, no actual bonding took place in these models.

Recent Simulation Method

In this section the simulation method previously published by Yildirim *et al.* is examined due the fact that this method is used in this research and the research preceding this work. Yildirim *et al*. used this method first in 2011[41] later adding to it in 2015[48] in collaboration with precursory research. Simulations were performed using the FE simulation software ABAQUS®. The method used a Lagrangian frame but includes a damage model to elevate the former issues of hyper-extended meshes resulting in model failure. When comparing this method to the previous two, it is found to yield the most promising results.[41] When a material point fails in accordance to a damage model

prescribed, that point is deleted from the calculation. In the Lagrangian simulation without this addition, a point expiring high strains would be tracked, extending and distorting the mesh; however, with the damage model that point is simply deleted when it exceeds the failure parameters, not forcing the mesh to distort and fail. In addition to this, Yildirim *et al*. added a method of modeling interface bonding. It stands to reason that particle bonding is the competition between the elastic energy of rebound that remains in the system after plastically deforming material and the interfacial bonding energy between the two bodies throughout the impact event.[33] It is not possible to know the interfacial bonding energy; therefor, interface bonding is modeled by defining an effective interfacial bonding strength parameter, constant along the entire interface. If the nominal stress at the interface exceeds this parameter, then there will be separation. The bonding strength parameters were based on the tensile strength values of the materials, a similar method is used when modeling the dynamic fracture process.[49, 50] The bonding strength values can vary with different materials and surface conditions, which is important to note since CS has the ability to use a wide variety of materials. Through this simulation method, it is discovered that the total area of bonded interface varies throughout the collision. Elastic rebound and cohesive bond energy are in competition and bonding is achieved when the rebound energy cannot overcome the cohesive energy of the material. It is seen in **Figure 7** that during elastic rebound the bonded interracial area decreases; if the rebound energy does not exceed the bonding energy, the interfacial region will come to rest with increased bonding area. This method simply provides a value that represents bonding but does not make any assumption about the exact nature of bonding, or variations in the value of this parameter with changing surface morphology

or impact velocity. However, this enables establishment of relationships between the critical velocity and bonding strength.[48]

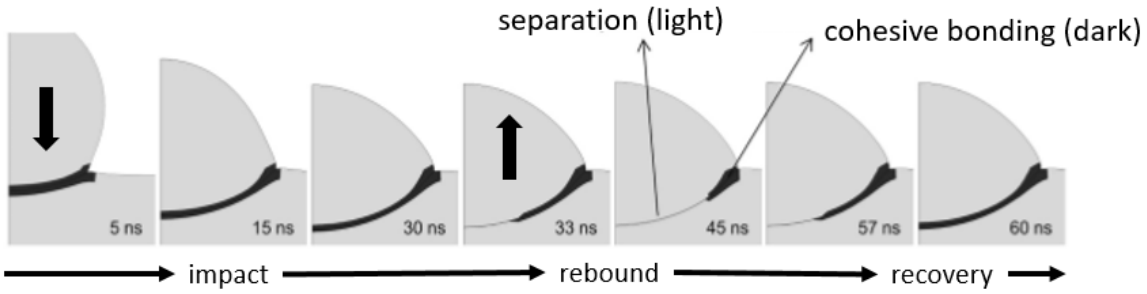

Figure 7: Simulation of the contact area at sequential times for impact with initial velocity of 750m/s of titanium particle and substrate. Note the changing bonding area during elastic rebound and the location of bonded area.[48]

When considering the material model used by Yildirim *et al*., the elastic properties are assumed to be linear and defined by the elastic modulus and the Poisson's ratio. Thermal properties are defined normally as well. The plastic deformation, however, is modeled using a non-linear isotropic material hardening plasticity model. The Johnson-Cook (JC) material model is commonly used to represent high-strain-rate deformations.[48] Unlike other flow stress models, like the Zerilli-Armstrong model which takes into account the grain boundary size, the JC model defines relationships between the flow stress, strain hardening, strain-rate hardening, and temperature softening effects.[51] This model will be explained further in a later chapter as it relates to current work as well. Material heating due to plastic deformation will be significant in this collision with large amounts of plastic deformation and high strain-rates.

Numerical simulations have led to many discoveries about the interactions that take place during the particle-substrate collision in CS, discussed earlier. Since the validity of these discoveries are dependent on the accuracy of the computational models,

experimental data is required in order to validate the models. Experimental data needs to be used to calibrate the models as well, through comparison of the experimental and simulated results. This method of calibration and validation was used by Dykhuizen *et al*.,[36] Yildirim *et al*.,[48] and later by Xie *et al*.[52]

Materials and Aluminum 6061

There is great interest in using thermal spraying to fabricate coatings and structures with unique functional properties by using many different material powders. To this end, CS has been used to accelerate and bond a wide variety of metals, like copper or high strength metals like titanium.[20, 22, 46] CS also has the ability to bond particles to substrates of dissimilar metals.[11, 53] Lastly, CS has the been used to create multi-functional coatings by depositing metal jacketed ceramic particles or multi-material metal powders.[54]

As mentioned, CS can be used to create free standing structures coatings or repair existing structure by adding material. There is an increasing interest in studying and evaluating the microstructure and mechanical behavior of relevant defense and aerospace alloys.[55, 56] CS deposits of ductile metals typically exhibit poor ductility and high hardness as a result of extensive cold working intrinsic to CS. Some resultant deposits may even contain varying degrees or porosity and inter-particle voids when compared to the conventionally processed materials.[57, 58] To improve the post deposition mechanical characteristics of CS deposits, heat treatments are often used.[59, 60] Extensive research has gone into optimizing this process of heat treating the unique CS deposits.[61]

Polycrystalline Aluminum 606l T6 alloy (AA6061) is a common material in many fields, including defense and aerospace applications. It has been used in CS to create free

standing structures and repair existing structures with promising results.[56, 62] AA6061 is comprised of 97.5% aluminum and other traceable elements (**Appendix B**)[63] and will be the topic of this study and work closely related.

Temperature Dependence

During static loading of ductile metals at an elevated temperature, there are observable degradations to the material properties. It has been shown that this is true for AA6061 at much lower temperature than other metals like steel. A study done by Summers *et al.* on the integrity and stability of AA6061 at effect of elevated temperatures, shows that there is a significant degradation, the largest difference taking place between 250 and 300 ℃.[64] In **Figure 8a** it can be seen that the Young's modules decrease nearly linearly with increasing temperature, except at around 200-300 ℃. In **Figure 8b** the yield strength also shows a significant decrease of about 140 MPa in this temperature region. A similar reduction is seen in the ultimate tensile strength in **Figure 8c**. Lastly, in **Figure 8d**, an increase in the ductile of the alloy is seen with increasing temperatures. This region with significant change in properties is the temperature threshold where the material undergoes charges in its dislocation and recrystallization mechanism. This change in microstructure evolution is likely the cause of the drastic changes in properties exhibited in **Figure 8**.[65]

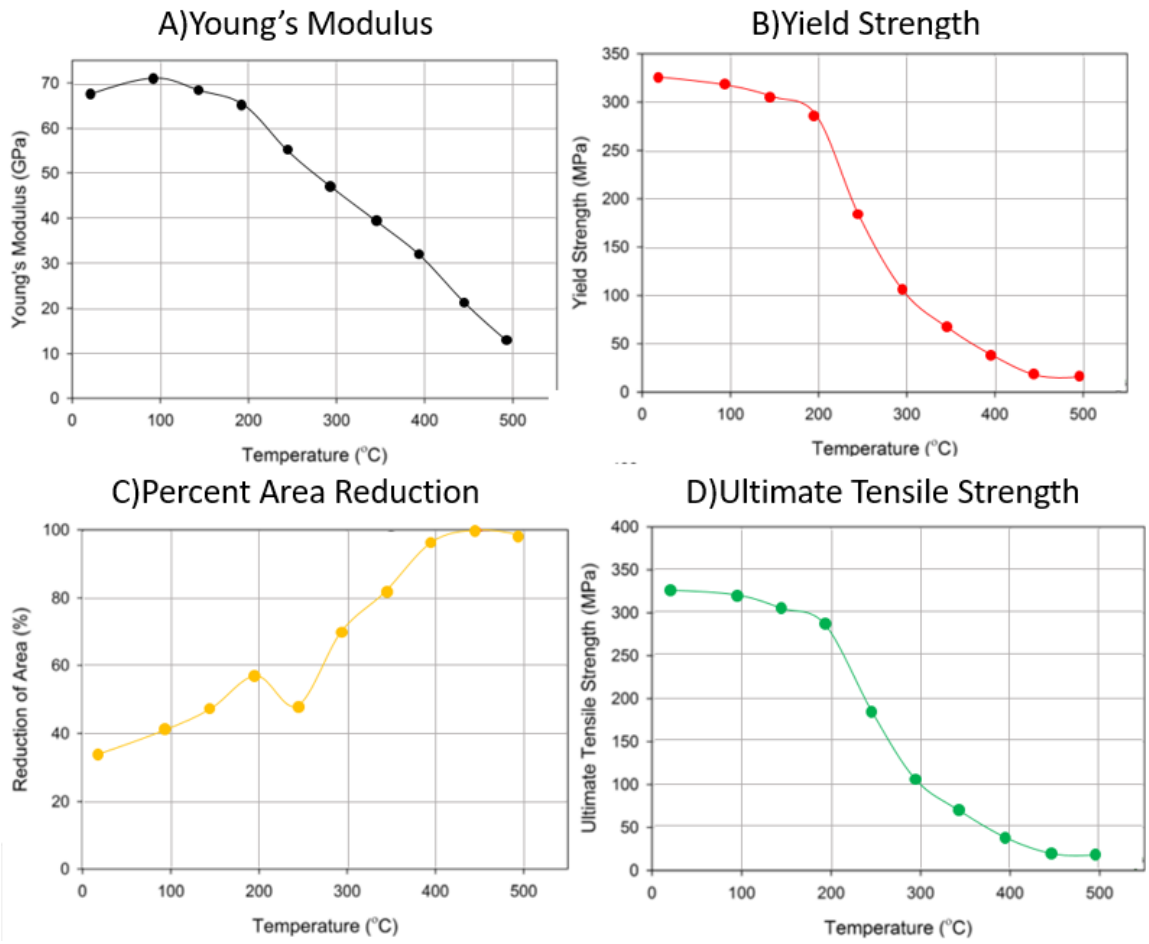

Figure 8: Changes in material properties with increasing temperatures during static loading. A) Shows the Young's modulus, B) yield strength, C) the percent reduction in area, which is indicative of ductility and D) ultimate tensile strength with increasing temperature for AA6061.[64]

However, CS is a high-strain-rate deformation process resulting in strain-rate hardening. To help understand this unique process, experimental and simulated data are studied together. Some of the most important factors in determining the critical velocity of bonding during CS is the temperature and thermomechanical properties of the particle and substrate materials. This leads to the assumption that the temperature affects the quality of CS deposits.[20,66] It is also well known that hardness is related to temperature. The effect of the substrate temperature has been studied; it has been reported that the deposition efficiency and adhesion strength increases with substrate heating, despite

increases in oxidation due to heating.[67,68] In 2017, Arabgol *et al.* studied the effects of increasing the substrate temperature for a variety of CS particles through experimentation and simulation. It was determined that heating the surface could lead to decreases porosity in the final structure, by allowing more deformation in the substrate compared to the particle.[69] Increasing the temperature has positive effects due to the increase in the total energy of the system. This increase in energy supports greater deformation and fluid-like flow at the interface and leads to metallurgical bonding as a result, through the removal of larger amounts of the inhibitive surface oxide layer.

Aluminum Oxide Surface Film

Bare metal surfaces often develop oxide films when exposed to the oxygen in the atmosphere. Oxide film growth on these metal surfaces are very rapid and can depend on the temperature.[70] AA6061 is no exception, there are assumed to be a surface oxide film, of at most 5 nm, on exposed surfaces. As previously discussed, the oxide film has a potentially large effect on the impact and subsequent bonding phenomenon in CS. The oxide free interface exposed during particle-substrate collisions results from the extreme deformation of the particles and substrate resulting in the creation of important pure metallurgical bonding locations. The breaking up of the thin native oxide layer, present on surfaces exposed to air, is required for pure metal-on-metal interactions and inter-particle bonding. Critical velocity has been shown to be influenced by the surface oxidation of the particles.[38, 71] Yin *et al*. finds that it is true that some oxide is extruded to the rim during the collision however, not all the oxide can be removed.[72] Oxide is found to be largely absent from the periphery but abundant in the center (**Figure 5b**). This suggests that bonding is present in larger amounts at the oxide free periphery regions.

This residual oxide layer in the center acts as an obstacle, preventing direct contact of metals and metallic bonding. It is seen through simulation that the center region of the interface is more likely to rebound from the residual elastic energy, due to there being an absence of cohesive bonding, which deteriorates or completely severs the bonds formed at the edge, significantly effecting the strength of the particle bond (**Figure 7**).[48, 73] Assumptions based on these findings suggest that thicker oxide layers will result in increased critical velocities and that smaller particles, having a larger surface to volume ratio, will have increased critical velocities.

It is known that the surface oxide growth will be affected by the temperature at which the material is exposed to. Jeurgens *et al.* studied the effect of temperature on the growth of oxide on freshly exposed surfaces of pure aluminum using x-ray photoelectron spectroscopy.[70] The aluminum oxide film growth rate will increase with increasing temperature above 400 ℃. Below this temperature, after the initial fast oxide film growth, the rate becomes virtually zero. Below 400 ℃, the oxide layer reaches a limiting thickness which increases with increasing temperature (**Appendix A**).[70] The surface oxide film will be a function of the temperature environment on flat bulk materials, with increased temperatures producing increased oxide thickness. The oxide layer thickness will be affected by elevated temperature, however below 400 ℃ the exposure time of the material will not have an effect of the thickness because it will reach a limit.[70]

The metallic particles in CS are also exposed to these high temperatures and will develop surface oxide films as a result. A study of these oxide film thickness on aluminum powers was performed by Trunov *et al.* They performed analysis on individual particles, evaluating the percent of aluminum oxide after exposing them to different

extreme temperatures (**Appendix A**).[74] The oxide percentage of the particle will increase with increasing temperature environments in distinct stages. Starting at 600 ℃ the oxide percentage will increase to a higher point and settle there, below this temperature the percentage remains constant.[74]

Previous Work

This report can be considered an extension of the work performed by Xie *et al*.[52] The following will be a review of that research. As discussed, the extreme material science behind the microscopic collision events that take place during the CS process is not well understood. Experimental observation of these events was previously challenging due to the fact that CS particles are generally 10-100 μm in diameter and their interaction with target substrates are less than 100 ns. In CS, large numbers of particles are accelerated per second in order to develop the bulk deposit structure, this further complicates *in situ* observation of particles. Obviously, each particle in a spray will have different impact parameters such as velocity, mass, size, temperature, shape, and angle. Computational modeling is used to overcome these obstacles and provide vital insight into particle impacts, however experimental data is still required to calibrate and validate these simulations to ensure that conclusions drawn accurately represent CS. In this publication, they present a method for experimentally observing well characterized single particle impacts *in situ* and the resulting particle micro-structure postmortem.

The study focuses on AA6061 particles with an average diameter of 19.3±5.3 μm. The acceleration and collision of single particles are observed in a highly controlled system called the advanced laser induced projectile system (α-LIPIT). Further

explanation of this process can be found in a later chapter, as it is used in this work as well. The experiments focus on accelerating AA6061 particles into two distinct substrates, sapphire and mirror polished AA6061. Sapphire is used as a target substrate to provide a near-ideal hard surface. Sapphire has modulus significantly larger than aluminum, so the majority of plastic deformation occurs in the particle and leaves the substrate virtually intact.[52] These particles can then be collected and observed using scanning electron microscopy (SEM). The results are used to improve simulation accuracy. Calibration of the simulation is greatly improved because the initial impact parameters are well recorded and it is possible to observe the particles shape after its collision, those initial parameters can then be run in the model and the resultant can be compared and calibrated to the experimental results. Aluminum on aluminum impacts are also performed to simulate the CS process. Using the α-LIPIT system, observations of single particle collisions are performed with the unique advantage of knowing the initial impact parameters and resultant dynamics of each particle, which had previously been unattainable.

Aluminum 6061-Sapphire Impacts

Sapphire has a shear modulus of 148 GPa compared to aluminum 6061 alloy's modulus of 26 GPa.[75] It can be assumed that most plastic deformation occurs in the particle when it impacts a sapphire substrate. Xie *et al*. performed AA6061 particle collision using the α-LIPIT system over a range of impact velocities, from 50 to 950 m/s, and particle diameters. Rebound velocity as a function of impact velocity can be found in **Figure 9a**. Rebound velocities increase linearly with increasing impact velocities until 120 m/s V_{TP}, after which the rebound velocity fluctuates with no distinctive trend.

Postmortem particles were collected and their deformed shapes can be seen in **Figure 9b.** There is increasing deformation with increase kinetic energy. A distinct transition from a linear increase to a more scattered rebound velocity at an impact speed of 100 m/s, indicated by V_{TP} is shown in **Figure 9a**. This velocity is where the entire particle experiences plastic deformation, as a result of more than half of its mass experiencing deformation. Cross sectional studies were performed using xenon plasma focused ion beam (FIB) milling. The differences in microstructural changes between particles impacted at 530 and 660m/s can be seen in **Figure 9d, f**. The particle impacted at a higher velocity shows viscous-fluid features crossing over grain boundaries, unlike the particle impacted at 530 m/s, which shows this only in the lower region of the particle, at the impact surface if at all. It is concluded that for particle velocities exceeding 550 m/s, the pressure experienced is so great that a microstructural collapse is induced and results in a hydrodynamic state inside the particle during collisions with a sapphire substrate. The onset of the viscous flow of material in the particle contributes to the increased rebound speeds experienced at higher impact velocities. The viscous flow of material in the impacting particle will reduce the rate of plastic deformation allowing for more elastic energy to be recovered, producing a higher rebound speed. This data collected is also used enhance simulations of these particle collision.

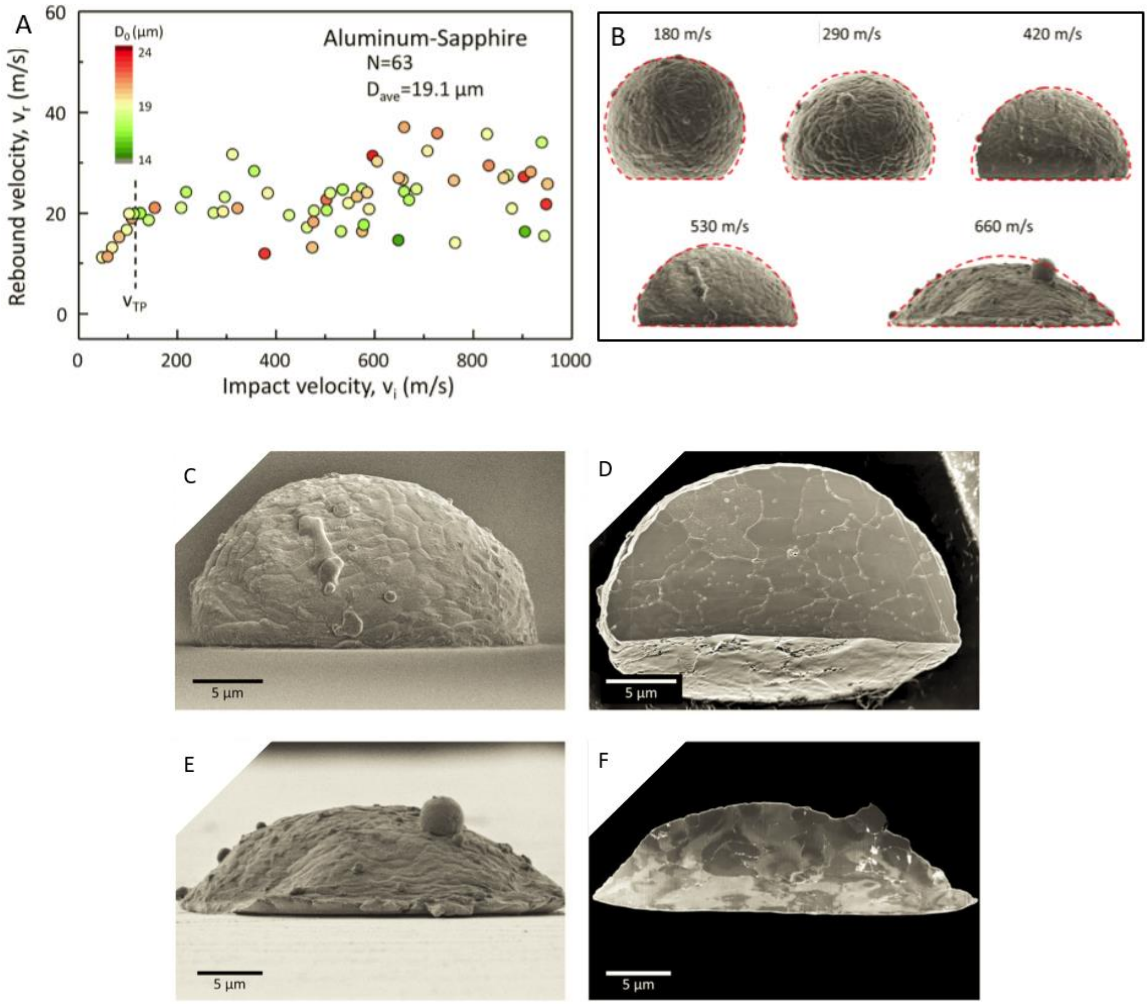

Figure 9: AA6061 micro particles impacting a sapphire substrate. A) A trend in the rebound velocity as a function of impact velocity. B) Side view SEM images of the particle collected after impacting sapphire at various velocities. The red outline represents the simulation results using the optimized parameters. C, E) Cross sectional images of particles deformed at 530 and 660m/s, respectively. D, F) High contrast SEM images of the cross sectioned particles.[52]

Simulation

Simulation of the particle collision is still required to understand what is happening during the extreme deformation of the particle, even though the α-LIPIT provides the unique ability to precisely observe the particle's impact and post impact parameters. Particle impact is modeled using the method discussed in a previous section, which is a Lagrangian frame including a material damage model and cohesive bonding

criteria. The simulation method is improved upon by the Applied Mechanics and Tribology Laboratory at Northeastern University, in collaboration with this work. The model uses three-dimensional large-deformation continuum mechanics with strain-rate dependent and isotropic plasticity. The simulation takes into account the material heating, the effects of temperature, and the heat transfer within the material as well as a material failure criterion and cohesive zone modeling.[76] A bilinear version of the JC flow stress σ_y model (**Equation 1, 2**) is used to perform these simulations to accommodate the temperature T, plastic strain ε_p, and plastic strain-rate $\dot{\varepsilon}_p$ increase seen at strain rates higher than $10^3 s^{-1}$.[77,78]

$$\boldsymbol{\sigma_y = \left(A + B\varepsilon_p^n\right)\left[1 + C\ln\left(\frac{\dot{\varepsilon}_p}{\dot{\varepsilon}_0}\right)\right]\left[1 - \left(\frac{T - T_R}{T_m - T_R}\right)^m\right]} \quad \textbf{(1)}$$

$$\boldsymbol{C = \begin{cases} C_1 \text{ and } \dot{\varepsilon}_0 = 1 & if\ \dot{\varepsilon}_p < \dot{\varepsilon}_C \\ C_2 \text{ and } \dot{\varepsilon}_0 = \dot{\varepsilon}_C & if\ \dot{\varepsilon}_p > \dot{\varepsilon}_C \end{cases} \text{with, } C_2 > C_1} \quad \textbf{(2)}$$

Here, the environment temperature is T_R, the melting temperature is T_m, and the reference strain is $\dot{\varepsilon}_0$. The equation variables include A, B, m, and n. **Equation 2** represents an additional increase in the yield stress when the plastic strain rate is greater than the critical plastic strain rate, $\dot{\varepsilon}_c$. The material properties and optimized equation variables used in the presented simulations are seen in **Appendix B**.[52,79] It should be noted that there is a large dependence on temperature according to this model. The JC model constants are optimized to match the deformed particle shapes, seen as a red outline in **Figure 9b**, thus calibrating the simulation to the experimental results. With these computational models, observations of the variable yield stress, internal strains, and temperatures are possible. It is found that particle deformation is largely influenced by

material hardening due to large strains and strain rates, which results in rapid increases in the yield stress in over 90% of the particles volume, for impacts greater than 300m/s. Furthermore, rapid decrease in yield stress is observed in impacts greater than 480m/s due to the particle experiencing fluid-like behavior in some regions.[52] **Figure 10a** shows the trend produced by this simulation method with its updated parameters compared to the experimental data. It can be seen that the simulation data closely matches the trend observed experimentally, thus validating the accuracy of the parameters and the simulation's ability to recreate CS collisions.

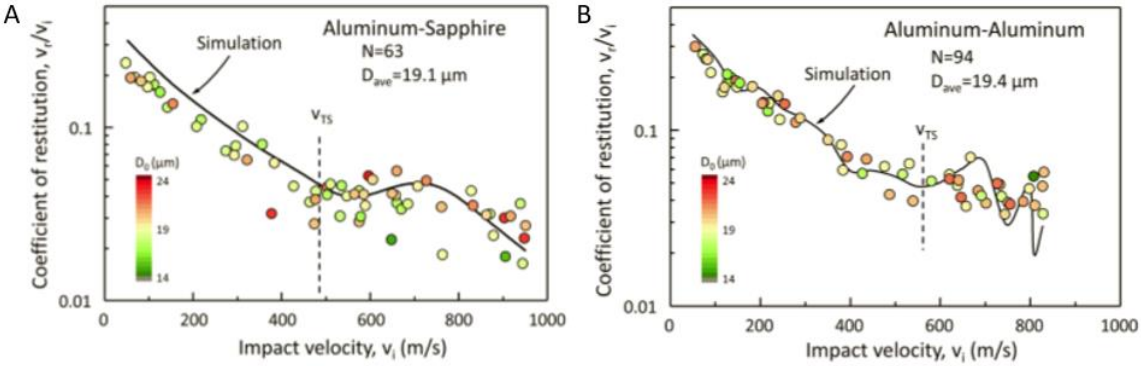

Figure 10: Impact velocity vs. the coefficient of resititution, which is the impact velocity divided by the rebound velocity, on a logerithimc y-axis. Superimposed is the trend line that is the result of the simulation with the optimized variables. A) AA6061-Sapphire impacts. B) AA6061-AA6061 impacts.[52]

Aluminum 6061- Aluminum 6061 Impacts

Xie *et al.* also studied AA6061 micro particles impacting polished AA6061 substrates experimentally, using the α-LIPIT system, and theoretically using the simulation method described. During these impacts, the collision is more complex due to the plastic deformation of the substrate, therefor not used for calibration of the simulation, however, this experimental data can still be used for validation of model parameters (**Figure 10b)**. The overall trend in rebound energy over a range of initial

velocities is similar to aluminum impacting sapphire (**Figure 11a**). However, the transition from linearly increasing rebound energy to constant and varying rebound energy is slightly higher due to the fact that the ductile substrates dissipates energy through plastic deformation while providing elastic relaxation in addition to the particle's reaction. In the intermediate region of impact velocities, again there is no observable increase in rebound energy. This indicated that the high strain-rate plastic deformation is capable of absorbing the increases in kinetic energy in this range. Once the slope starts to increase again at 600 m/s, material softening begins to dominate strain hardening. With increasing impact velocities, the critical velocity of 840±10 m/s is observed, where the rebound velocity is zero and the particles are bonded to the substrate.

Post impact cross sectional SEM images of bonded particles are seen in **Figure 11f-i**. The presence of the material jet at the rim can be seen in the high velocity collision that resulted in bonding, which supports the presence of interfacial instabilities hypothesis. **Figure 11a** shows a high speed impact without bonding, the rim of this crater shows a rounded edge. In **Figure 11 c, d, e** where there is bonding of the particle, the outer rim of the crater shows a sharp edge, or a jet of material originating from the substrate. The presence of this jet only when the particles are bonded leads to the conclusion that material jetting is required for bonding. The cross sectional SEM images show that the grains are highly compressed, especially closer to the interfacial region, resulting in a gradient in grain size throughout the structure. Through observations of the rebound energies, it is determined that cohesive zone bonding cannot be the only mechanism for bonding. There is an estimated 21 J/m^2 of dissipated energy when bonding at the critical velocity, which is much higher than the cohesive interfacial energy

of aluminum which is >1 J/m^2 (**Figure 11a**).[80, 81] This indicates that there must be other mechanisms taking place to dissipate energy, such as local melting at the interface.

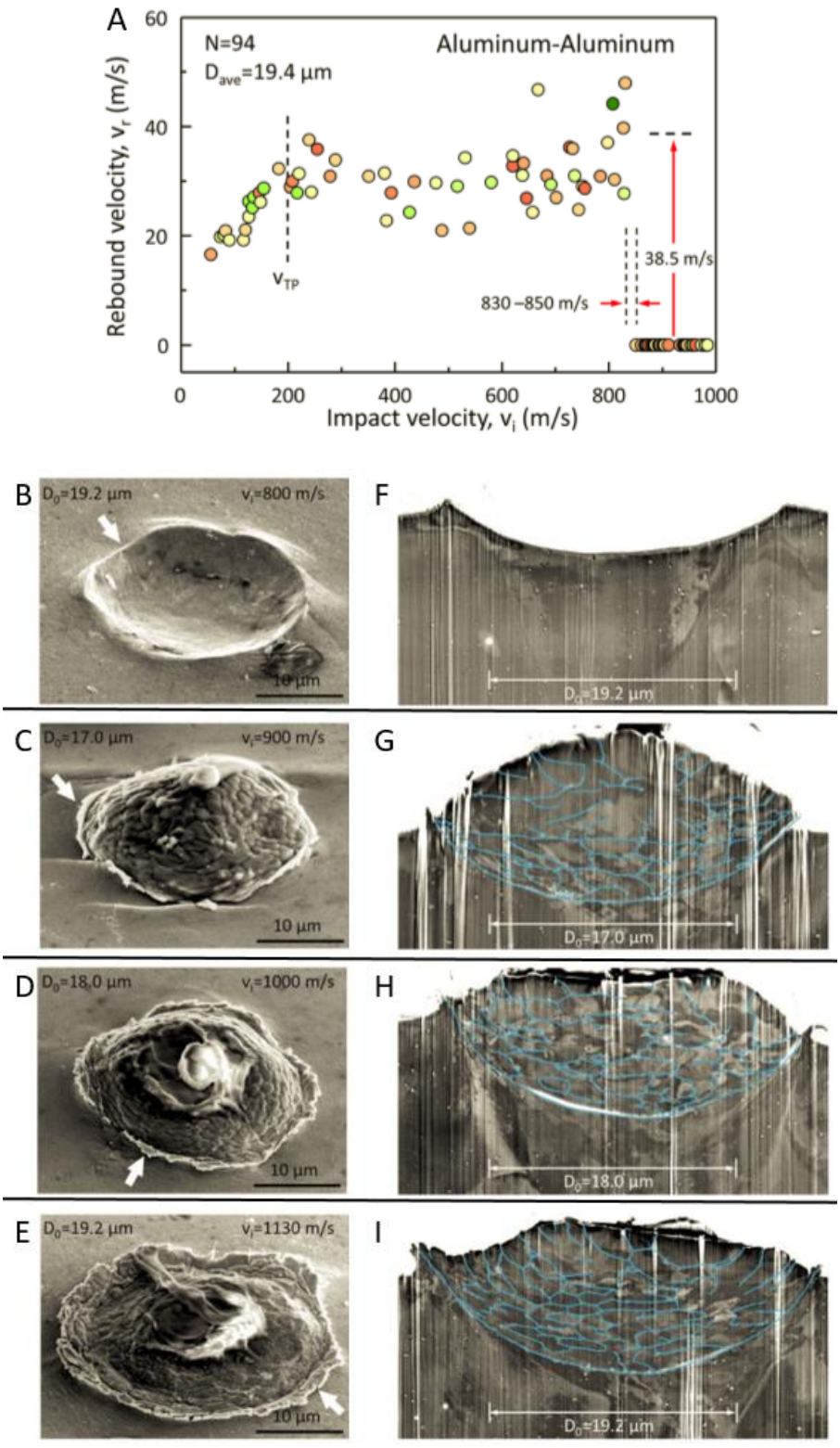

Figure 11: A) Trends in the rebound velocity as a function of impact velocity for AA6061 micro-particles impacting a polished AA6061 substrate. B-E) Same magnification SEM images of particles with varying impact velocities, 800, 900, 1000, and 1130 m/s. F-I) Contrast enhanced cross sectional SEM images of the impact sites and bonded particles.[52]

Related Work

Recent work performed by Gangaraj *et al.* on particle impacts of various materials to like material substrates is similar to the work presented in this thesis and by Xie *et al.* The same particle acceleration and experimental data collection method are used by this group, the α-LIPIT. Their main focus was on further enhancing the simulation technique and providing coupled experimental data to understand the formation of the material jet, which is widely believed to be required for particle bonding. Similar simulation techniques to those previously discussed are used, with the Johnson-Cook flow stress model being selected to simulate the nonlinear stresses present in ABAQUS®. This simulation, however, was aimed at understanding the effect of the pressure shock wave produced during impact. To capture the hydrodynamic behavior of the particle upon impact, the Mie-Grüneisen equation of state (**Equation 3**) was used.[82] This defines pressure (P) as a function of density (ρ) and the initial energy per unit mass (E_m), with $\eta = 1 - {\rho_0}/{\rho}$ representing the volumetric compressive strain, Γ_0 a material constant known as the Grüneisen constant, C_0 is the bulk speed of sound. The equation is linear in energy and assumes a linear relationship between the shock velocity and the particle velocity. The simulation parameters can be found in **Appendix B**.[83]

$$P = \frac{\rho_0 {C_0}^2 \eta}{(1-s\eta)^2}\left(1 - \frac{\Gamma_0 \eta}{2}\right) + \Gamma_0 \rho_0 E_m \quad (3)$$

Unique to these simulation and experimental observation is the capturing of ejected material. Above the critical velocity, there is very fast lateral jet-like material ejection. Based on this observation, the formation of the jet and plastic ejection of material is critical to bonding, similar to the hypotheses previously discussed. **Figure 12** shows simulations of copper-copper particle-substrate impacts at the critical velocity. During this simulation the ejection of material, formation, and eventual fracturing of the jet can be observed. **Figure 12a** shows the normalized temperature values throughout the impact of a copper particle. Even at the peak the plastic work induced temperature rise never reaches the melting temperature for the material tested directly contrary to simulation results of previously published literature.[22, 34-37, 48] This leads to the conclusion that melting is not responsible for the formation of the material jet. Using new temperature dependent hypothesis, they developed a trend defining the critical velocity's dependence on temperature, and conclude that increasing particle temperature leads to greater flattening and less penetration upon impact, and decreases in critical velocity in a manner that follows a square root dependency (**Appendix A**). In **Equation 4** V_c is the critical velocity.

$$V_c = V_{c,room}\sqrt{1 - (T - T_{room})/(T_{melt} - T_{room})} \quad (4)$$

The yield stress throughout the impact, in **Figure 12b,** reviles that the adiabatic shear localization does not reach a compromising value until after the material begins to form the jet structure. This leads to the conclusion that the localization of forces at the interface is not responsible for the formation of the jet, however it may be a consequence of the jet formation. The conclusion of this work is that the pressure shock wave is what is responsible for formation of the jet, which is required for bonding. The compressive

shock interaction with the particles leading edge results in the material jetting and mixing flow that exposes the pure surfaces for metallurgical bonding sites, essential for adhesion of the particle to the substrate. Furthermore, they were able to develop a more refined prediction equation for finding the critical velocity, by basing the critical velocity off of the onset of a pressure wave able to form the material jet.[83] In **Equation 5,** *d* and *n* represent the particle size effect and *B* is the bulk modulus.

$$V_c \approx 0.15\sqrt{\left(\frac{d}{d_0}\right)^{-n}(1-(T-T_{room})/(T_{melt}-T_{room}))\frac{B}{\rho}} \quad (5)$$

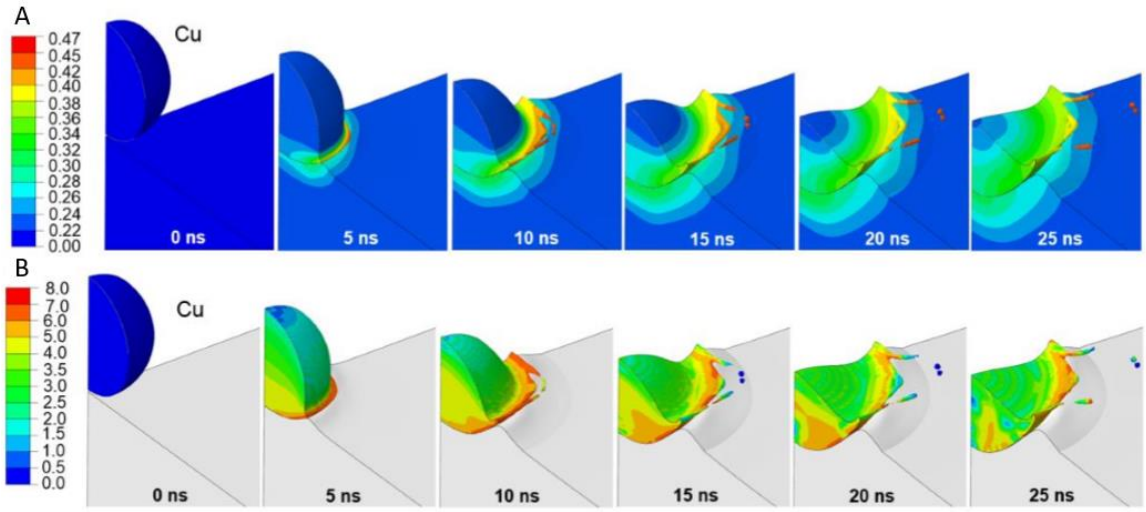

Figure 12: A) Instantaneous temperature distribution normalized with the initial temperature at sequential time steps throughout the impact of a copper particle to a copper substrate at the critical velocity. The melting temperature is never reached indicating melting is not required for jet formation and ejection. B) Instantaneous yield stress distribution normalized with the initial yield stress at sequential time steps throughout the impact of a copper particle to a copper substrate at the critical velocity.[83]

The α-LIPIT system provides the capability of performing highly controlled single particle impact tests to simulate the CS deposition process. Impact velocities are easily observed, ranging from less than 50 to over 1,000 m/s, along with other parameters, yielding well characterized collision events which can be analyzed

postmortem. The documented characteristics and results from the impacts are used to validate and calibrate numerical simulations, enhancing their accuracy further, allowing insight into the internal mechanisms occurring during cold spray. In this study, different parameters were able to be controlled, however there are many other variables that affect the CS process, such as temperature, impact angle, and oxidation layer thickness. The α-LIPIT has the capability to control and vary those parameters as well, in order to yield further experimental results; which can be used to calibrate simulations or provide insight into the underlying material science occurring during this complex process.

CHAPTER 2

METHODS

Discussed here is the method first used by Lee *et al.*[2] and later modified for the work done by Xie *et al.*[52] and Gangaraj *et al.*[83] The advanced laser induced projectile impact test or α-LIPIT system will be explained in detail here. AA6061 microparticle powder was received from United Technology Research Center. The particles were annealed at 230℃ for 1 hour and then sieved to reduce the particle size distribution, the goal being an average size of 20μm. AA 6061-T6 was received from McMaster-Carr in bulk. 5mm x 5mm blocks are used as the target substrate. The blocks are mechanically polished using grinding papers and abrasives. The smallest abrasives used were 0.5μm silicon particles yielding a surface roughness around this value. Any computation simulation work is performed by Applied Mechanics and Tribology Laboratory at Northeastern University in collaboration with this work. Simulations are performed using an identical method to that used in Xie *et al.*[52] For cross sectional images, xenon plasma focused ion beam milling (Helios PFIB, FEI) was used to slice the micro particles. Then images of the milled particles are taken with SEM.

α-LIPIT System

The α-LIPIT system is used to perform mechanical characterization tests. The system allows for high velocity and HSR testing on the micron scale, similar to the premise of CS, micro particles are accelerated to supersonic speeds. This method permits the selection of single particles and characterization of several parameters during flight and collision, which is impossible with a thermal spray device. The particle can be accelerated to velocities of up to 1,100m/s without any noticeable laser damage and its

impact velocity and angle, with respect to the surface normal direction of a target substrate, can be measured as well as the rebound characteristics, if there is no bonding.

The particle is accelerated by rapid expansion of an 80μm thick elastomeric film made of cross-linked polydimethylsiloxane (PDMS) on top of a gold film and supported by a thin glass plate, which make up the ablation substrate. An excitation laser pulse (5–8ns pulse duration, 1064nm) is created by using a Nd:YAG laser (Quanta-Ray INDI-40-10-HG, Spectra-Physics). The ablation substrate, holding several micro particles, is placed on the focal plane of the laser. The ablation substrate moves independently, allowing for micro particles to be located and placed precisely at the focal point of the laser. Particles resting on the ablation substrate are viewed through a 10x magnification live camera on the vertical axis, which is also used to measure the particles diameter prior to ablation. The rapid transformation of gold to gas produced by the laser ablation results in local expansion of the PDMS and launches the resting particle at velocities proportional to the laser power (**Figure 13a**). The PDMS layer also serves to isolates the particle from the laser during ablation. The particles flight is quantified using a multiple-exposure photograph taken by a low-noise and high-quantum-yield digital camera (C11440-22C, Hamamatsu Photonics) using ultrafast white light pulses, at known intervals, producing images similar to **Figure 13b**. The velocity can be calculated by measuring the distance in between the particle locations and dividing by the known time in between light pulses, which is controlled by the α-LIPIT system.

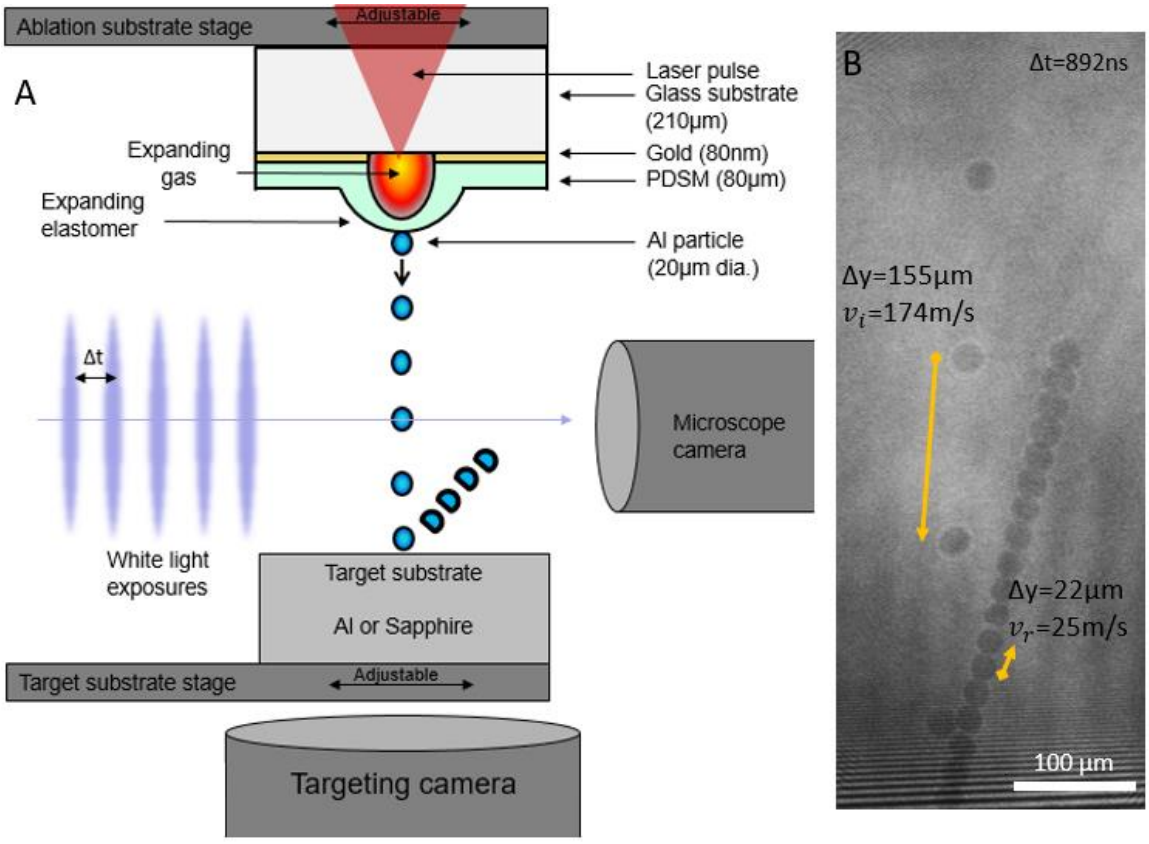

Figure 13: A) α-LIPIT system schematic. B) Image produced by the α-LIPIT system, from which the impact and rebound velocity can be measured.

To create the ablation substrate, a thin microscope cover glass plate is sputter coated with an 80 nm thick gold film. Then, a two part PDMA (Sylgard 184, Dow Chemical) is mixed with a ratio of 10:1 and spin coated on the gold coated glass to ensure that the thickness is approximately 80μm uniformly across the glass plate. The substrate is then cured at 200 ℃ for one hour. The AA6061 micro particles are mixed with isopropanol, creating a transport solution. A single drop of solution is applied to the ablation substrate. The liquid solution is spread over the surface by placing a small piece of lens cleaning paper over the drop, thus spreading the particles and preventing clustering while the isopropanol evaporates. With this method the particles are spread

enough, and the laser ablation is accurate enough to accelerate one particle with high aiming accuracy with each ablation.

Temperature Chamber

In order to expose the particle and substrate to elevated temperatures, a chamber surrounding the location of the collision event is constructed in such a way that the α-LIPIT system can function as normal. The temperature chamber is constructed from AA6061, allowing temperatures to reach over 300℃. Experiments are performed at 100, 200, and 300℃. The chamber is equipped with four heaters mounted on the inner walls. The temperature is regulated through a positive feedback loop controlled by a temperature reading from the thermocouple placed on the inner wall of the chamber. However, the temperature of the wall will not be the temperature of the particle due to the air inside, thus the controller must be set to a higher temperature than the desired impact temperature, usually 25 ℃ higher. There are two more thermocouples placed on both the target and ablation substrate stages (**Figure 14a**). The average between these two is taken to be the temperature of the particle, since the particle's flight path is in between these two locations. The difference between the two stages does not exceed 10 ℃ and usually settles to less than 5 ℃.

The particles impact two different target substrates, as discussed before, sapphire and polished AA6061. When impacting sapphire, the particles must be recovered after the collision in order to observe the extent of deformation. When capturing the rebounding particles, a cover is placed over the impact area in the temperature chamber with a cap having a 1 mm diameter hole in line with the focal point of the ablation laser. Particles travel through the hole and impact the sapphire substrate, the impact velocity is

measured before entering the cover (**Figure 14b**). To image the post mortem particles, the cover is removed and since the cover blocked other particles from entering, there is only the measured particle present under the cover. That is then removed from the target substrate surface with a PDMS cube, which is soft enough to no damage the particle and adhesive enough to lift it from the surface. The particle and PDMS substrate are then coated in a thin gold layer to enhance SEM image quality. The SEM used is a Magellin-400. Images of the top are taken on a flat imaging stub and images from the side are taken by placing the PDMS substrate on a 90-degree surface stub.

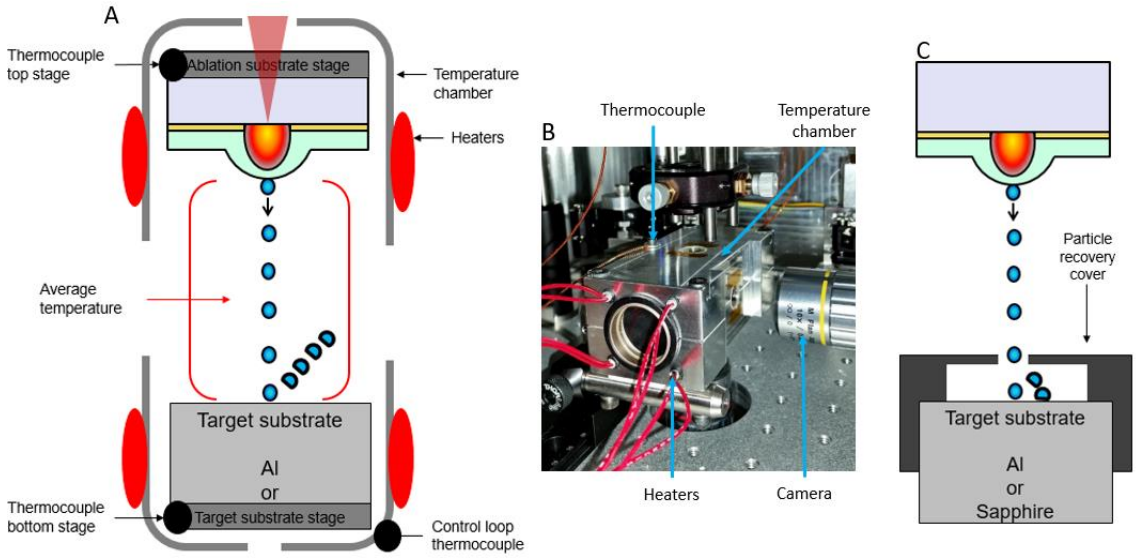

Figure 14: A) Schematic of the temperature chamber incorporated into the α-LIPIT system. B) Image of the temperature chamber within the system. C) Schematic of cover used to recover particles after collisions.

Surface Oxide Film

As discussed, the presence of the surface oxide film has an effect on the bonding capabilities of the CS particles. A 2-5 nm thick oxide film is native to exposed AA6061 surfaces. An additional 20 nm and 10 nm layer of aluminum oxide is deposited on the target substrates with atomic layer deposition (ALD) postdoc, David Gonzalez. 20 µm

AA6061 particles are accelerated at a range of velocities to observe the trend and the critical velocity, where bonding is initiated, using the α-LIPIT at room temperature unmodified.

CHAPTER 3

SPECIFIC AIMS

Aim 1: Temperature Dependence

Study and define the dependence of the high-strain rate single particle impacts on the environment's temperature by performing impacts at various elevated temperatures and observing the change in the dynamic response as well as observation of the postmortem particle structure.

Aim 1 proposes to validate the theory that elevated temperatures will affect the material response of the aluminum particles during impact. By elevating the temperature of AA6061, the material will soften allowing for increased movement or destruction of dislocation within the micro particles. However, thermal softening will be in competition with strain-rate hardening. Therefor, the extent of the temperatures effect needs to be determined. Temperature increases during impact could lead the material to surpassing the melting temperature in a high temperature environment. There have been simulations on elevated temperatures of particles and experimental data of elevated substrate temperature, however none for an elevated system, including both particle and substrate, which will more closely resemble the CS process. Furthermore, Xie *et al*. performed experiments with the α-LIPIT to measure 20 μm diameter AA6061 particle collisions at room temperature,[52] which will provide a controlled comparison to effect the high temperature environment has on the particle-substrate collision event.

Specific to this aim, the dynamic response against a rigid sapphire surface will be conducted in order to isolate the effects of the collision to only the particle. This provides less complex data that is used to calibrate and validate the simulations of these impacts at

elevated temperatures using the unique capabilities of the α-LIPIT system. Looking at the JC equation that governs the flow stress of the material in this computational simulation (**Equation 1, 2**), there is a large dependence on temperature. By calibrating the simulation of the particle impacts with data collected at variable temperatures, we will be able to gain further confidence in the simulation's ability to model the impacts and subsequently further confidence in the results derived from the simulations about the internal material dynamics during the supersonic impact.

It is hypothesized that there will be increased plastic deformation or flow of material during impacts. Also there will be increased bonding ability resulting from the increase in flow of material, this will be in the form of a lower bonding critical velocity.

Aim 2: Aluminum Oxide Surface Film

Study and define the effect of a bonding barrier in the form of an increased surface oxide film on the high strain-rate impact of aluminum 6061 micro particles on the a polished AA6061 material substrate with a thickened surface oxide film.

Aim 2 proposes to study the effects of having a bonding barrier between the two bonding elements, the AA6061 particle and substrate, in the form of the surface oxide film. The native oxide film present on exposed AA6061 surfaces is approximately 2-5nm thick. Since Xie *et al*. performed experiments with the α-LIPIT to measure 20 μm diameter AA6061 particle impact at room temperature with only the native oxide film thickness,[52] this will provide a control comparison to effect thicker oxide layer has on the particle-substrate collision event. Increasing the thickness of surface oxide film on the aluminum substrate will increase the bonding barrier and effect the ability of the particle to bond to the substrate during its impact. In order to bond, more energy will have to be

put into plastic flow to extrude the surface oxide to the rim. Furthermore, by decreasing the ability of the particle to bond to the surface the cohesive energy will be decreased, resulting in an increase in the available energy for rebounding.

It is hypothesized that by increasing the surface oxide film thickness the particles will require more energy, in the form of impact velocity, to bond to the substrate. The critical velocity will increase. This is due to the brittle surface oxide layer blocking essential aluminum on aluminum interactions between the particle and substrate decreasing the cohesion between the two materials.

CHAPTER 4

RESULTS AND DISCUSSION

The capabilities of the α-LIPIT system have already been shown to accurately simulate the collision events present in CS process.[52, 83] In these experiments, *in-situ* observations of micro particle impacts and rebounds were recorded using the α-LIPIT system described in the previous sections. This capability has proven to be useful in augmenting computational simulations and understanding the complex high-strain-rate dynamics of these collisions.[52] In these experiments micro particles approximately 20 μm in diameter of AA6061 are accelerated at a wide range of velocities and impacted upon a target substrate. To examine different aspects of the impact phenomenon two different target substrates are used, a polished sapphire piece and a mirror polished AA6061 substrate. The impact and rebound velocities are then captured by the α-LIPIT system and recorded. With this information, an understanding of the energy dissipation and deformation during impact is gained. Furthermore, post mortem particles can be observed using this testing system. Unique to this research, a heating chamber has been added to the α-LIPIT in order to capture and observe data about collisions at an elevated temperature. As discussed, elevating the temperature has many different effects on ductile metals like AA6061. These effects include material softening, a higher energy system, closer to the melting temperature, and increases in surface oxidation at very high temperatures.[70, 74] The following are the results of the α-LIPIT experiments performed at elevated temperatures with AA6061 microparticles impacting both a sapphire and AA6061 target substrate.

High Temperature Aluminum 6061-Sapphire Impacts

Results

With the α-LIPIT and the heating chamber, several experiments at elevated temperatures have been performed with AA6061 particles impacting a sapphire substrate. The sapphire substrate is selected due to its high modulus and hardness compared to the micro particles. This substrate can act as a near-ideal hard substrate. This isolates the micro particles' reaction to the HSR deformation, allowing for the assumption that all deformation takes place only in the impacting particle. The rebound velocities for collisions at room temperature (23),100, 200, and 300 ℃, can be seen in **Figure 15a-d** with unique color scaling representative of the slight variations in the initial diameters of individual particles. The scattered data developed from recorded impact and rebound velocities from numerous experiments was smoothed using an unweighted adjacent averaging method, represented by **Equation 5. Figure 15e** represents the smoothed data, using a range of 20 data points, (r = 10).

$$data_{(i)} = \frac{data_{(i-(1:r))} + data_{(i)} + data_{(i+(1:r))}}{2r+1} \qquad (5)$$

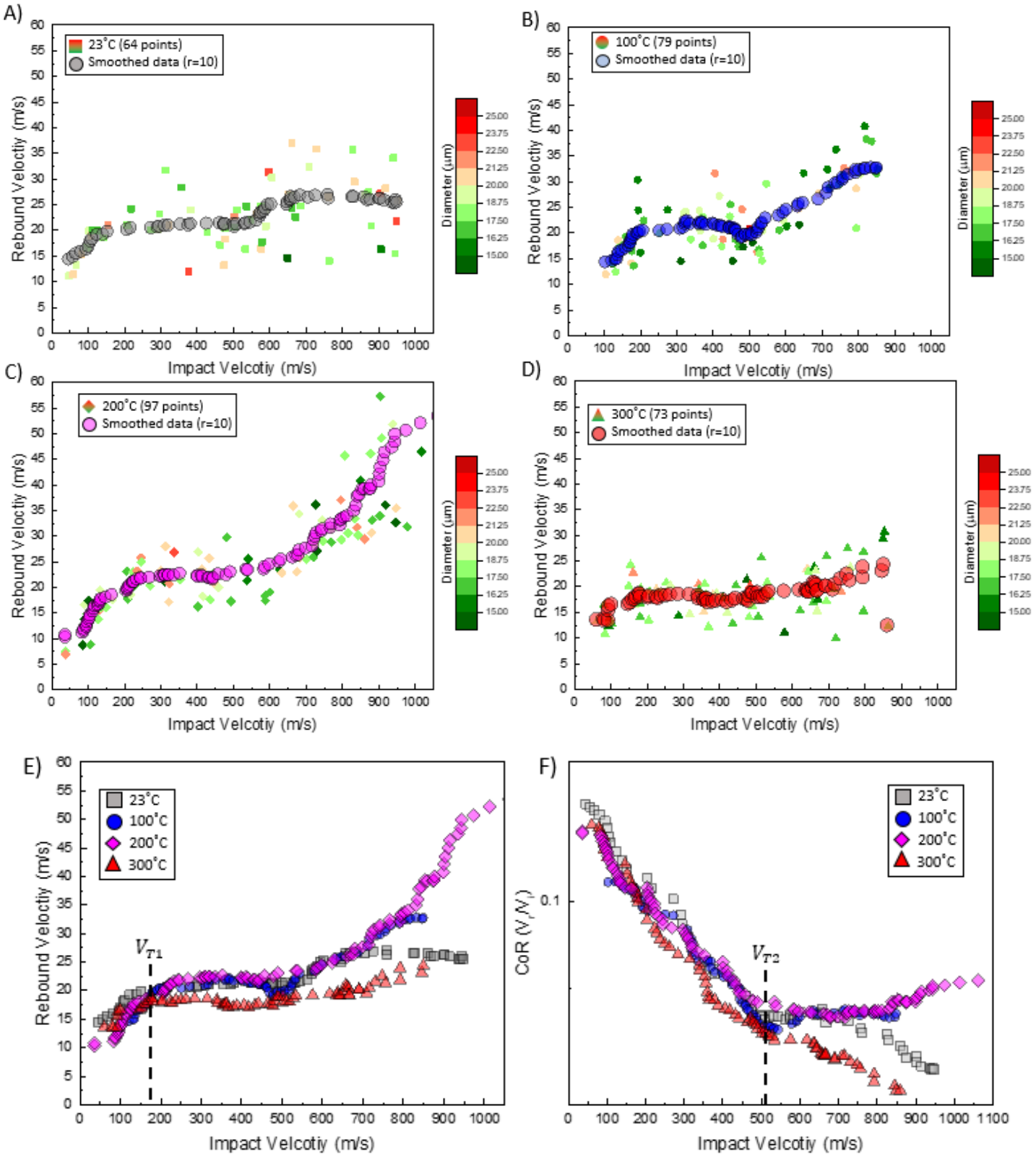
A)
23˚C (64 points)
Smoothed data (r=10)
B)
100˚C (79 points)
Smoothed data (r=10)
C)
200˚C (97 points)
Smoothed data (r=10)
D)
300˚C (73 points)
Smoothed data (r=10)
Rebound Velocity (m/s)
Impact Velcotiy (m/s)
Diameter (μm)
E)
23˚C
100˚C
200˚C
300˚C
V_{T1}
F)
V_{T2}
CoR (V_r/V_i)

Figure 15: Temperature depended AA6061 micro particle impacts on a sapphire substrate. A,B,C,D) 23,100, 200, and 300°C, respectively, with color scaled initial diameter size dependence. E) data from all 4 temperatures smoothed using Equation 5. F) Smoothed data represented as the coefficient of restitution, which is the rebound velocity divided by the impact velocity, log y-axis.

Figure 15e shows that the first transition zone is approximately 150-200 m/s, marked by V_{T1}. This transition area is seen at all temperatures at roughly the same impact velocity. The trends move from a linearly increasing to a slope of nearly zero, until the second transition is reached. V_{T2}, at an impact speed of 525 ± 50 m/s. V_{T2} can be more easily seen in **Figure 15f,** a plot of the coefficient of restitution. In the first region, at impact velocities lower than V_{T1}, the rebound speed increases linearly, which would be expected if there was proportional energy absorption by the particle with increasing impact energy. After V_{T1}, the rebound velocity begins to settle for all temperatures around 20 m/s except 300°C, at which it settles at lower rebound velocity of 18 m/s. This change from a linear growth trend marks the ability of the particle to deform plastically absorbing a large fraction of the impact energy. In this region, the rebound velocity is equivalent for a range of impact velocities because the strain rate hardening of the micro particles is enough to overcome additional impact energy.[52] The impact energy is absorbed by the particle and dissipated effectively at all temperatures in this impact speed region except 300°C, where the rebound energy is even lower. This implies that the thermal softening caused by the heating at 300°C has a greater effect on the deformation process. This corresponds well with the data presented earlier, where the largest difference in the yield strength and modulus for AA6061 was between 200 and 300°C.[64] At this high temperature there is less elastic energy recovered meaning more plastic deformation must be taking place due to the decreased strength caused by thermal softening.

The second transition happens when the majority of the particle experiences plastic deformation and the energy can no longer be absorbed due to the initiation of viscous flow in the material, reducing plastic deformation and increasing the rebound velocities.[52] There is a good match for this transition at all temperatures, except at 300℃, where it difficult to distinguish. However, this is to be expected due to the material softening at this higher temperature. With the softer material at elevated temperatures, there is a decrease in the energy required to cause the majority of the particle to plastically deform, inflating the impact velocity of V_{T2} at 300℃. After V_{T2}, there are increases in the rebound velocities at all temperatures, however at room temperature the rebound velocity seems to level off again. The increase in rebound velocity after V_{T2} is likely due to the particles reaching some maximum deformation based on their respective temperature, with by far the most deformation present above 300℃. Through cross sectional images is **Figure 9**, this transition is where this is an observable collapse in the grains to the particle, indicating internal viscous flow of the material. By further increasing the impact energy, the rebound energy also increases since the particle cannot absorb more energy after viscous flow has begun.

The α-LIPIT also provides the ability to capture the particles after they have impacted the sapphire surface to observe their deformed shape. **Figure 16** shows various images of particles at different temperatures and impact velocities. It can be seen that at velocities above V_{T1} (the first column) less than half of the particle is deformed. At V_{T2}, about half the particle is deformed, and this begins the next phase where the rebound velocities start to increase again. Above V_{T2}, the particles develop a lip around the outer

edge at all temperatures, corresponding well with the second transition in impact speed and can be considered an indication of this threshold (**Figure 15e**).

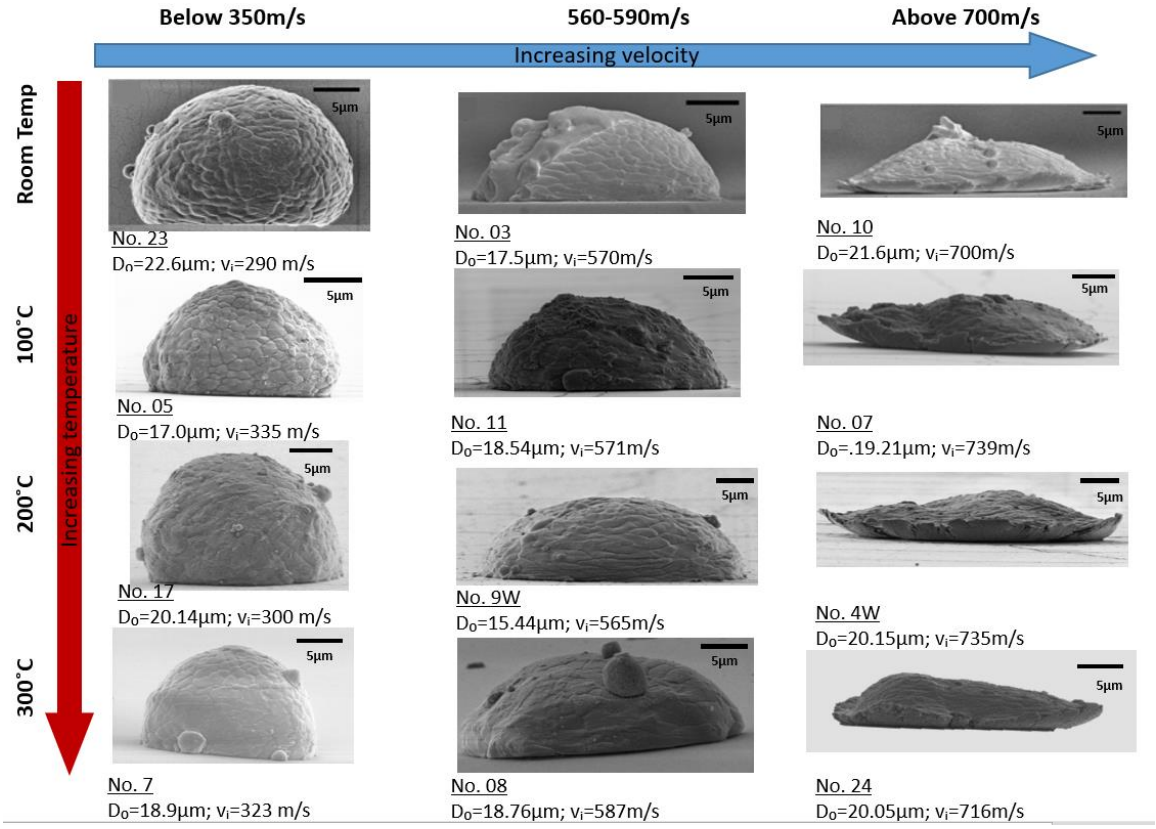

Figure 16: SEM images of particles after impacting a sapphire surface at various impact velocities and temperatures.

By measuring the initial diameter of the particle and the height of the particle after the collision, the flattening can be calculated ($\Delta D/D_0$). **Figure 17** shows the flattening ratio for particles at all temperatures. A linear increase in the flatting ratio is seen, which correlates well to the conclusion from Xie *et al*.[52] As expected, with increasing temperature there is increased softening of the material leading to more flattening or deformation at higher temperatures represented by a steeper slope in **Figure 17.** Furthermore, **Figure 17** shows that at a ratio of 0.5 normalized deformation, the second transition happens, supporting the conclusion previously drawn by Xie *et al*. and reinforced by these results.

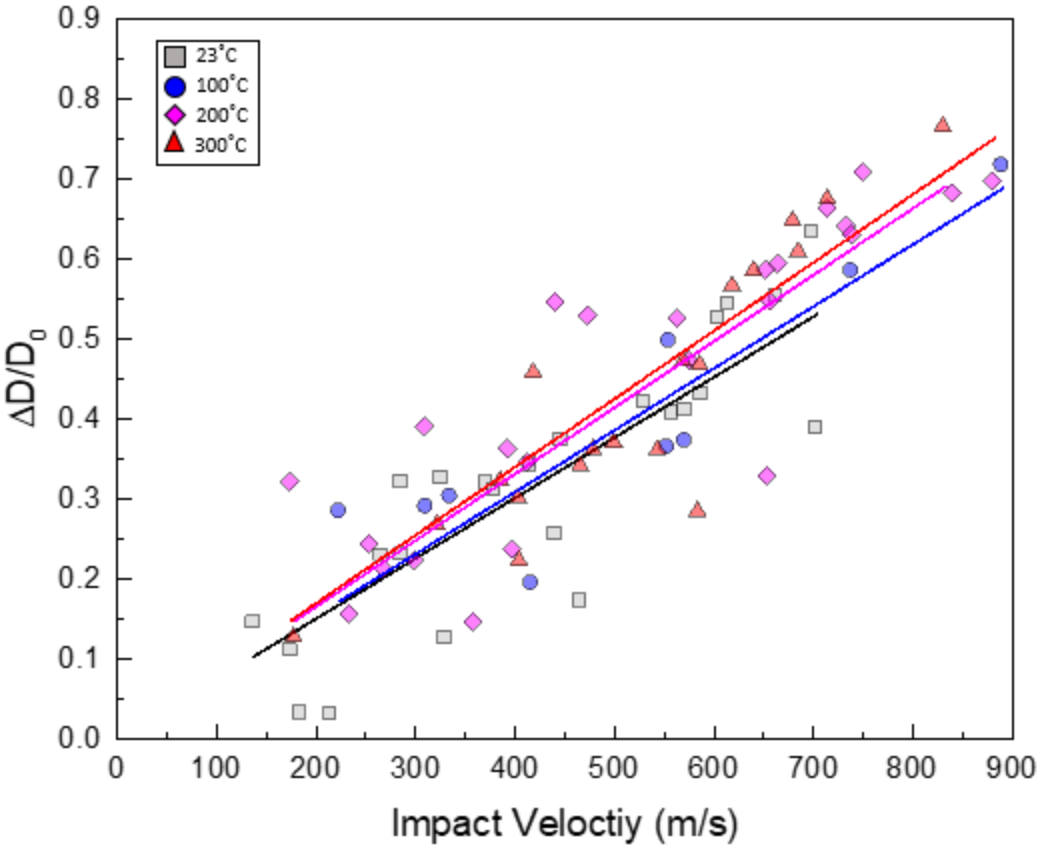

Figure 17: Plot of the flattening ratio or the normalized deformation of particles at various elevated temperatures and impact velocities. The linear trend lines are shown to highlight that the slope is increasing with increasing temperature. This is indicative of increased deformation at increased temperature and impact velocities.

At the second transition velocity, around 600 m/s, the particles the majority of the particle has experienced extreme deformation at all temperatures as indicated by a ratio greater than 0.5 (**Figure 17**), however past this impact velocity the particles also begin to form a jet region around the outer rim (**Figure 16**) at the same time the rebound speeds begin to increase again (**Figure 15e**). The significance of the jet region is explained thoroughly in the literature and is believed to be crucial for bonding. Gangaraj *et al.* found both experimentally and through simulation that upon impact with a surface at a high enough impact velocity the particles will produce a jet and from that jet, material will be ejected.[83] This α-LIPIT is unable to experimentally observe the material being

ejected, however **Figure 18** shows evidence of material loss from the jet region of the particles. The underside of the particles shows a roughened surface, which is indicative of some material being ejected and others being left behind. The surfaces of particles impacted below V_{T2}, show a flat and smooth surface. Above V_{T2}, like in **Figure 18** where there is a jet formed, the surface is roughened. It is known that above V_{T2} the particles experience viscous flow, this could be related to the formation of the jet and its ability to eject material. **Figure 18** also shows that with increasing temperature and similar speeds the roughness visually increases, potentially indicating greater material loss. This would be a cause of the dramatic increase in thermal softening above 200°C.

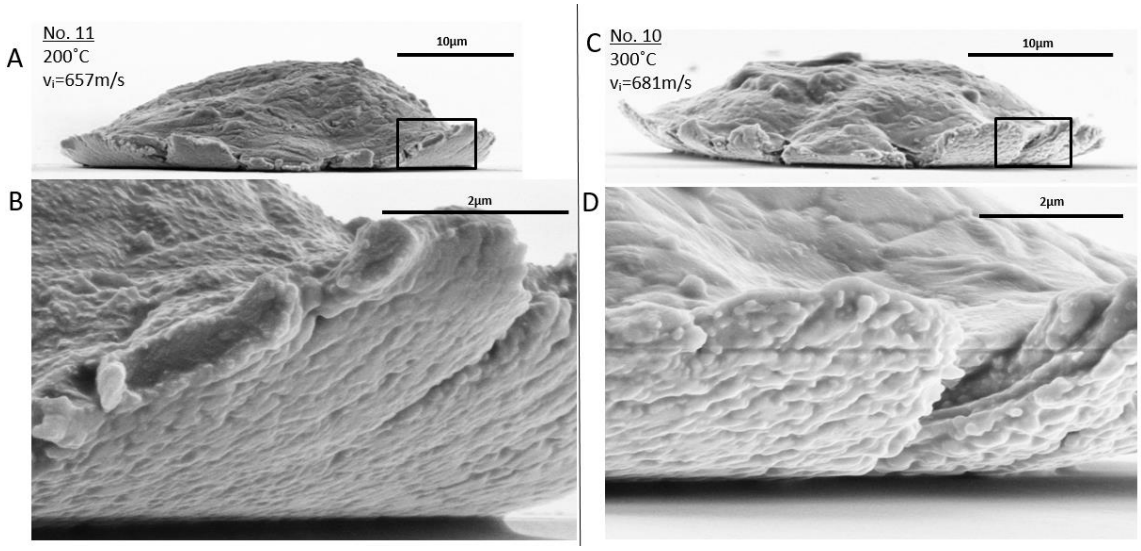

Figure 18: A) SEM image of a particle impacted at 200°C from the side. B) a high magnification of the boxed portion of A, highlighting the roughness of the exposed underside of the outer rim. C) SEM image of a particle impacted at 300°C from the side. D) a high magnification of the boxed portion of C, highlighting the increased roughness of the exposed underside of the outer rim.

Discussion

The results presented display the trends of the rebound velocity as a function of impact velocity (**Figure 15**), side view SEM images of deformed particles (**Figure 16**) allow for the measurement of the deformation ratio in **Figure 17** of numerous collision

events at various temperatures and impact velocities. This data is aimed at discovering the effect temperature has on the unique HSR deformation that takes place in CS. By having an ideally hard target substrate, sapphire, it can be assumed that the vast majority of deformation happens in the particle, effectively isolating the particle in these collision events. Through observation of the trends presented in **Figure 15e,** increasing the temperature to 200℃ has little effect on the rebound of AA6061 particles impacting a sapphire substrate below V_{T2}. However, at 300℃ there is a distinct change in the rebound velocity of these particles. This is supported by the nominal decrease in mechanical strength of AA6061 from 23-200℃ and the distinct decrease from 200-300℃. Thermal softening and the change in mechanical properties of the micro particles is responsible for the change in rebound energies above 200℃. Furthermore, it can be concluded that the temperature has little effect on the HSR deformation of these micro particles below 200℃. The trends in **Figure 15e** show that even at elevated temperatures, the second transition velocity still occurs at a deformation ratio of roughly 0.5, supporting the conclusion made by Xie *et al*. Further study of the particles post-mortem reveal that at this second transition velocity the particles' inner structure undergoes viscous flow internally and develop a jet region at the rim (**Figure 16**). Gangaraj *et al*. found that there was ejection of material at high velocities and from **Figure 17**, there appears to be evidence of material ejection from the roughness of the exposed under surface of the particle. This roughness increases with increasing impact velocity and increased temperature, eluding to increased thermal softening resulting in increased material ejection. There is likely a connection to the formation of the jet, subsequent ejection of material, onset of internal viscous flow, and the deformation ratio greater than 0.5

observed at all temperatures at V_{T2} of approximately 600 m/s. Whether the phenomena are caused by or simply correlated to each other requires further research, but it is known that all these phenomena happen at $V_{T2}$and for all temperatures, resulting in an increase in rebound energy. The material ejection phenomenon could further explain the increased rebound velocities occurring after V_{T2}. The ejection of material could contribute to increases in rebound velocity due to less mass needed to be moved. With more energy and less mass, the rebound velocity would increase at these high impact velocities. This conclusion would also explain the difference in the trends after V_{T2}, at room temperature and elevated temperatures (**Figure 15e**). The rebound velocities do not increase much with increasing impact velocity after V_{T2} at room temperature but 100 and 200 ℃ do continue to increase with increasing impact velocity. This could be caused by rises in material loss due to thermal softening. The thermal softening is not as great as it is at 300 ℃ where there is such a dramatic decrease in the material strength that the rebound energy is much lower. This is caused by much greater amounts of plastic deformation at high temperatures even though there is likely greater material loss. Lastly, it is important to note that the careful observation of AA6061 micro particle collisions with sapphire is an important technique used to calibrate and validate CS simulations (**Figure 10**).[52]

High Temperature Aluminum 6061- Aluminum 6061

Results

With the α-LIPIT and the heating chamber, several experiments at elevated temperatures have been performed with AA6061 particles impacting a polished AA6061 substrate. This substrate material presents a more accurate representation of the cold spray process. However, having a substrate of the same material as the impacting particle

will also complicate the system. There will be elastic and plastic deformation in both materials and changes in material properties in both as a result of the temperature increase as opposed to the previous section. Similarly, the rebound velocities for collisions at room temperature (23),100, 200, and 300°C, can be seen in **Figure 19a-d** with unique color scaling representative of the slight variations in the initial diameters of individual particles. The scattered data developed from recorded impact and rebound velocities from numerous experiments was smoothed using an unweighted adjacent averaging method (**Equation 5**). **Figure 19e** represents the smoothed data, using a range of 20 data points, (r = 10).

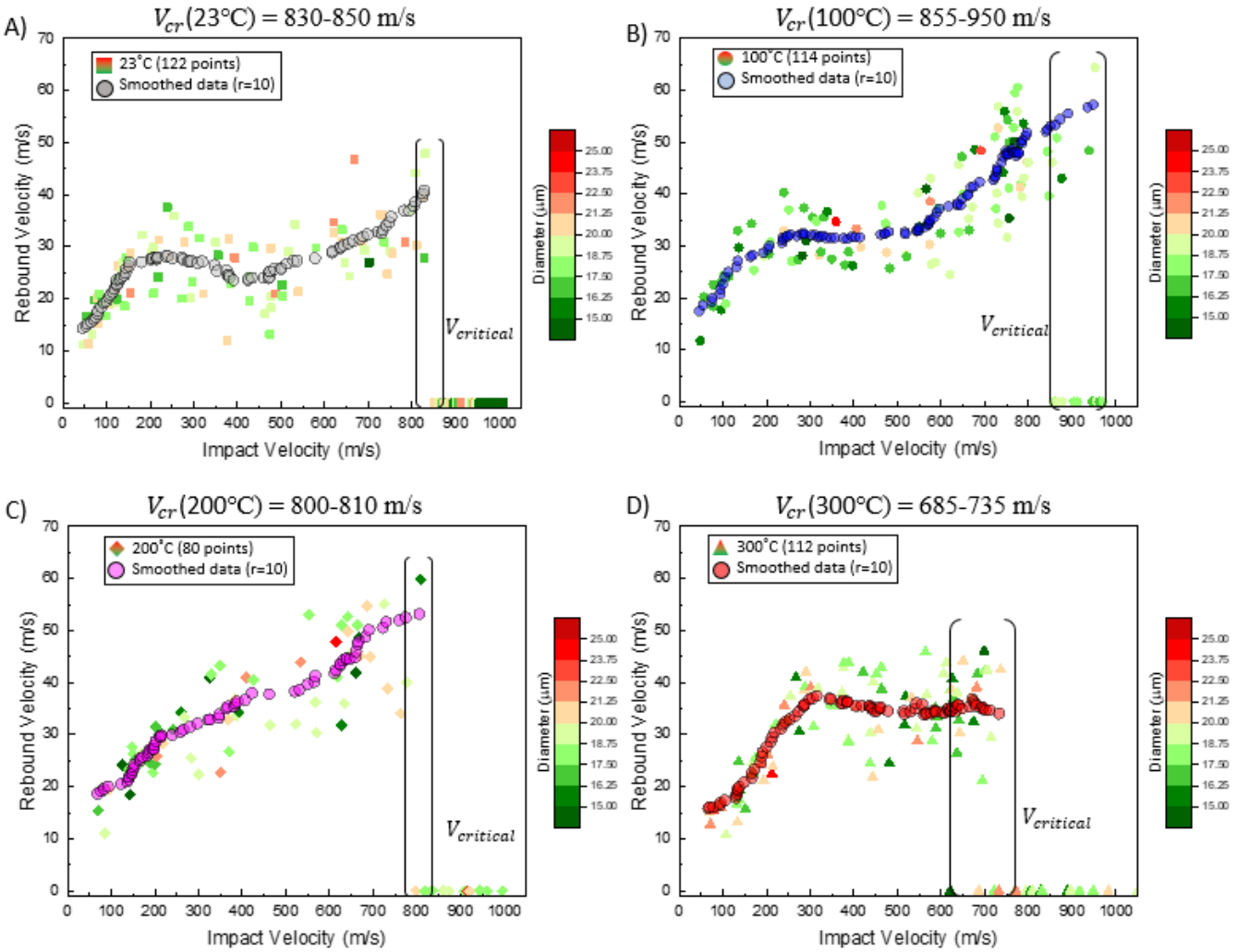

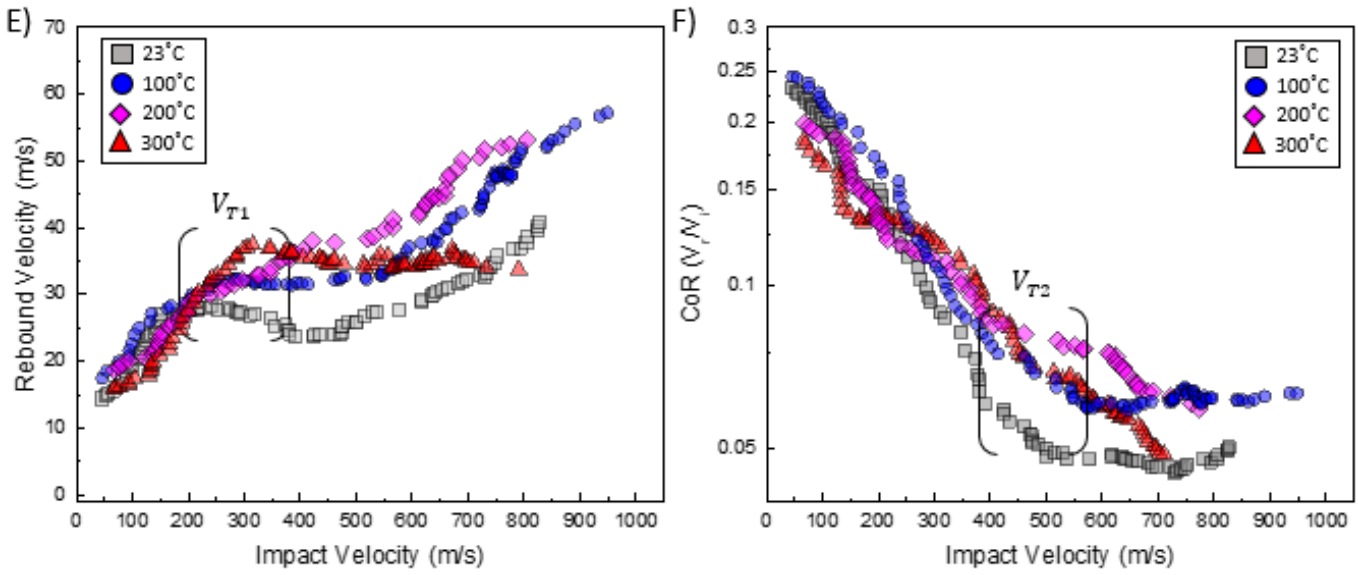

Figure 19: Temperature dependent AA6061 micro particle impacts. A,B,C,D) 23,100, 200, and 300°C, respectively, with color scaled initial diameter size dependence and the data smoothed using Equation 5. E) data from all 4 temperatures processed. F) Smoothed data represented as the coefficient of restitution, which is the rebound velocity divided by the impact velocity, log y-axis.

Figure 19e shows that the first transition zone is approximately 150-200 m/s, marked by V_{T1} for temperatures 23 and 100 °C and approximately 300 m/s for 200 and 300 °C. The trends move from a linearly increasing to a slope of nearly zero, until the second transition is reached. V_{T2}, which is again at different impact velocities for higher temperatures. V_{T2} can be more easily seen in **Figure 19f,** a plot of the coefficient of restitution, which again is seen to be different for the higher temperatures, which could be a result of the onset of internal viscous flow at a lower impact energy. In the first region, at impact velocities lower than V_{T1}, the rebound speed increases linearly with increasing impact velocity similar to that observed in the sapphire impacts, which would be expected. At room temperature and 100 °C the $V_{T1}$is much more obvious than at other temperatures. V_{T1} is more complicated to define at 200 and 300°C, the trend lines at these temperatures transition from linear growth to a different slope of linear growth at

approximately the same impact velocity as the lower temperatures. However, the transition to a zero slope appears to take place at around 400m/s, much higher than the lower temperatures. Furthermore, the rebound velocity at which this zero slope region occurs at higher rebound velocities for elevated temperatures and all AA6061-AA6061 impacts settle at a higher rebound velocity than the sapphire impacts. This is explained by the presence of elastic energy being recovered in not just the particle, as with the sapphire experiments, but also in the ductile substrate.[52] With thermal softening there should be less elastic recovery in collisions at a higher temperature, however that is not the case for elevated temperatures. (**Figure 19e**). On the contrary, the rebound energy at elevated temperatures are actually higher than at room temperature, with the highest being at 200℃. The decrease in rebound velocity from 200 to 300℃ can be attributed to the drastic decrease in thermal softening at this temperature range. At higher temperatures, the second transition happens at a lower impact velocity than the lower temperatures, indicating that there is more flattening as with the sapphire impacts, and easier onset of internal viscous flow which would be expected with greater thermal softening. After this second transition impact velocity, at all temperatures the rebound velocity begins to raise. This must be result of the maximum deformation achieved without bonding and internal viscous flow, because upon inspection of unbonded particle impacting a like-material substrate Gangaraj *et al*. and this work finds no evidence of jetting or material loss at impact speeds less than the critical velocity.[83] The final observation from **Figure 19e** is the change in the critical velocity for elevated temperatures. As expected and predicted by Gangaraj *et al*. the critical velocity decreases at increased temperatures. This is true for all but 100℃ which remains the same or slightly increases. The change in critical

velocity as a function of temperature can be seen in **Figure 20a** along with the predicted critical velocity by **Equation 5** presented by Gangaraj *et al*.

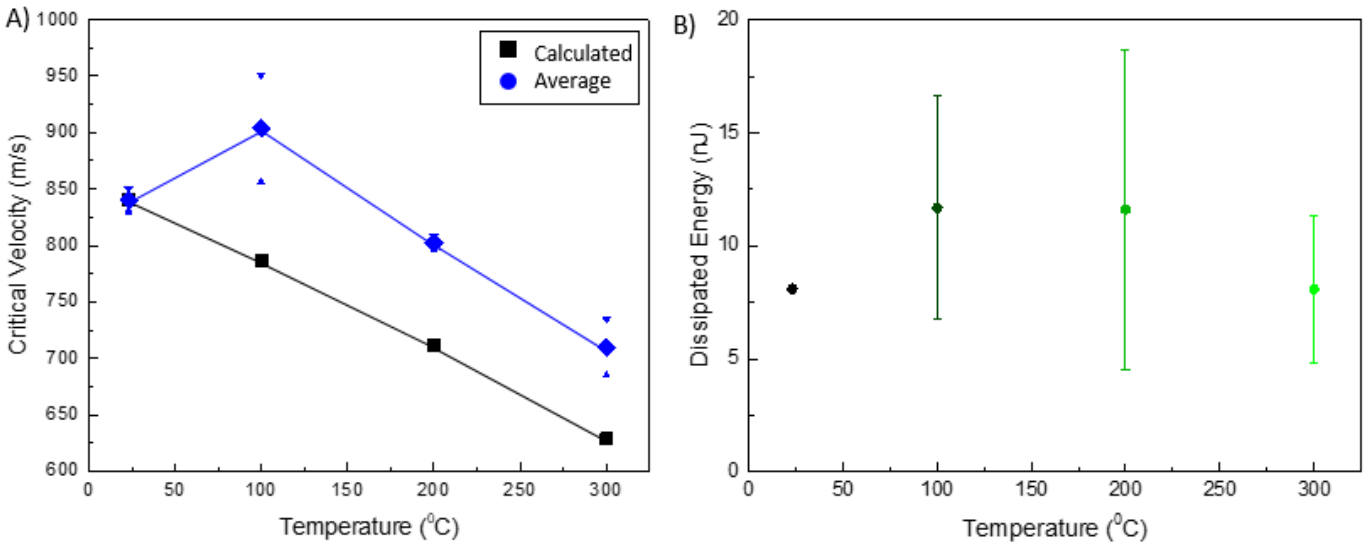

Figure 20: A) The normalized critical velocity as a function of temperature. In green, the predicted critical velocity from Equation 5. The leading coefficient was changed to 0.165 to account for the different material used and to get the normalized critical velocity to be one at the reference temperature (23°C). In black are the experimental results. B) the dissipated energy as a function of temperature. The dissipated energy was calculated for a particle of diameter 20μm with the rebound energy observed just prior to the critical velocity.

The rate of change of the critical velocity in the experimental data shows a good match to the numerical equation, however at 100°C the calculation and the data differ greatly, altering the predicted critical velocities for higher temperatures. **Figure 20b** demonstrates a calculation for the dissipated energy of the particles at different temperatures. The dissipated energy is calculated by **Equation 6** where m is the mass and V_r is the an average of the rebound speeds of unbonded particles with the highest impact velocity. This rebound velocity would represent the amount of energy that must be dissipated in order for bonding to occur. This value would also be indicative of the cohesive energy because it is roughly equivalent to the energy opposing cohesion at this impact velocity.[48]

There is an increase in amount of energy required to be dissipated with increasing temperature, and at 300℃ this energy returns back to approximately the same as room temperature.

$$E = 0.5 * m * V_r^{\,2} \qquad (6)$$

Lastly, as predicted in Xie *et al*. and Gangaraj *et al*. and confirmed by this data, the bonded particles at all temperatures show a distinct jet formation, which is crucial to bonding (**Appendix A**).

From the data presented in this section several conclusions are drawn that are both supported by previous findings and contrary to what would be expected. The critical or bonding velocity is decreasing with increasing temperature (**Figure 19e**), however this decrease does not take effect until the temperature is greater than 100℃ after which the rate of change in critical velocity closely resembles that of the equation presented by Gangaraj *et al*. (**Figure 20a**). Unexpectedly, the rebound velocities for all temperatures greater than room temperature are much higher. The rebound energies should be less because there should be increases in plastic deformation due to thermal softening, this is seen in the transition between 200 and 300℃ which is also where the largest decrease in strength takes place.[64] In **Figure 19e**, the second transition takes place at a lower impact velocity at higher temperatures. This could be explained by the increased thermal softening present at higher temperatures resulting in a lower impact energy being required to cause internal viscous flow, which previously had been the cause of the second transition.[52] Lastly, **Figure 20b** shows that with increasing temperature the energy required to dissipate for bonding is increasing as a result of the higher rebound velocities, although the critical velocity is decreasing. It would be expected that the bonding energy

would decrease because as the material softens it could become more fluid during a HSR deformation and material would be jetted and ejected more easily and result in bonding with less energy being required. However, this is not the case, from the high temperature experiments the energy required to be dissipated to result in bonding actually increases with temperature. This energy does decrease from 100 to 300°C (**Figure 20b**). If thermal softening at elevated temperatures cannot explain these unpredicted phenomena in AA6061-AA6061 impacts than there must be other factors contributing to this collision even not present in the AA6061-sapphire experiments and not predicted by simulations.

Additional Oxide Thickness Results

In order to further understand the variables, present in CS, it is possible to study the effect that the surface oxide layer has on the particle collision with the α-LIPIT. It has been widely theorized in the literature that oxide layer plays a significant role in the bonding process of metallic particle to a metallic surface (**Figure 3**).[23] This brittle oxide surface acts as a barrier between the chemically pure internal material in both the particle and the substrate. Bonding is thought to be governed by the ability of the collision to remove this oxide barrier and expose the pure material to each other for chemical mixing and metallurgical bonding. To gain understanding of the effect the temperature has on the CS collision the temperature was varied and the response was recorded to see how it changes with the changing variables. Similarly, in order to fully understand the effect of this oxide layer, we vary its thickness and, using the α-LIPIT, experimentally test the collision's response. **Figure 20** shows the dynamic response of HSR collision of AA6061 particle onto a surface of AA6061 that has a variable oxide thickness. The oxide

thickness was increased with atomic layer deposition (ALD). The data was smoothed with the same process as previous dynamic response trends.

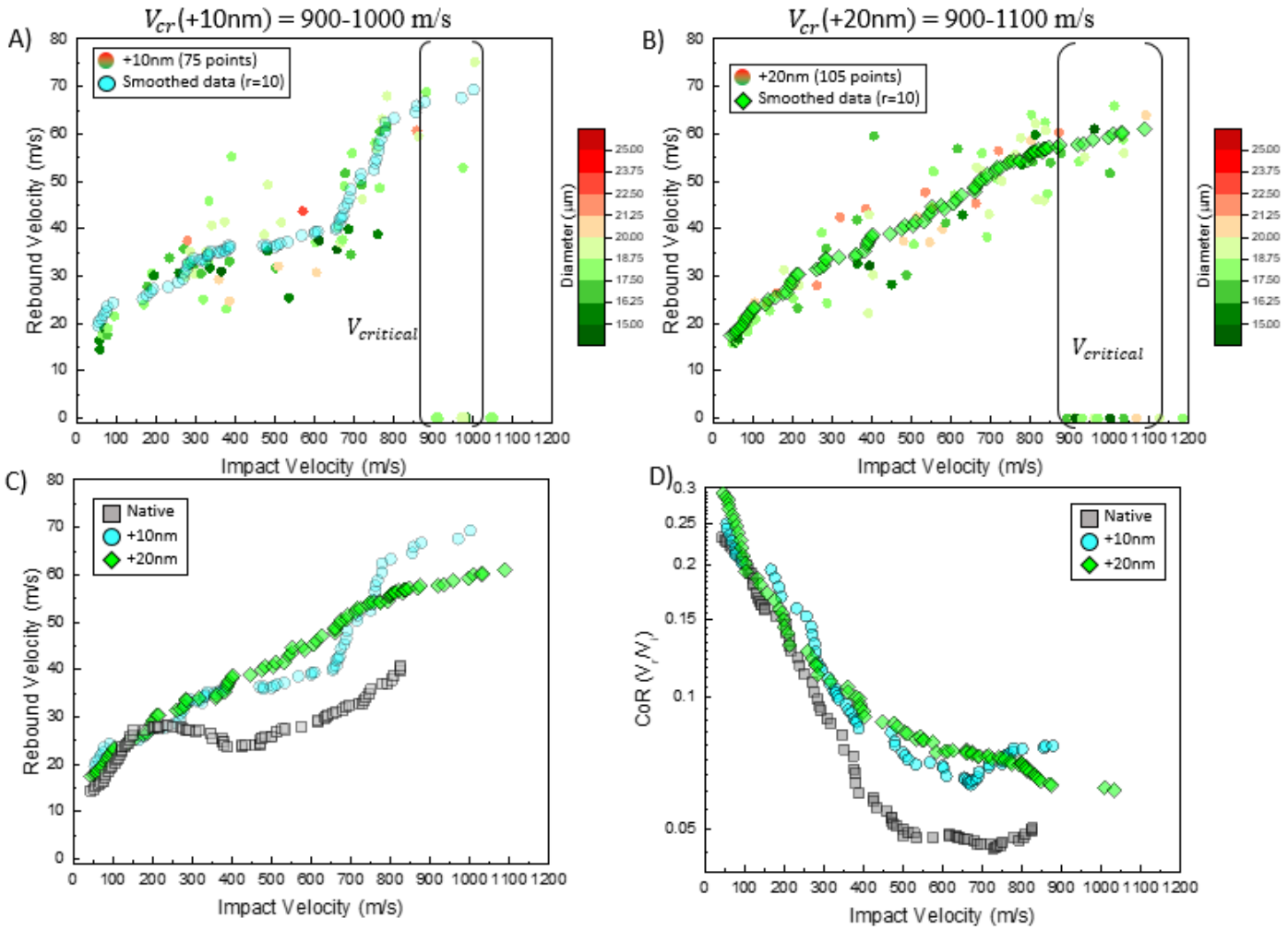

Figure 21: A, B) Additional 10 and 20nm applied to the polished impact surface a AA6061 substrate, respectively, with color scaled initial diameter size dependence and the data smoothed using Equation 5. E) data from both additional thickness experiments and the native oxide thickness (same as room temperature) experiments processed. F) Smoothed data represented as the coefficient of restitution, which is the rebound velocity divided by the impact velocity, log y-axis.

From the trends, there is a considerable rise in the rebound velocities when there is an increase in the surface oxide thickness. This fits in well to what was previously hypothesized about the effect of this layer.[71-73] When the surface oxide is increased it becomes more robust, it would then require more energy to break and expose the pure

material. Furthermore, an oxide is more brittle resulting in less plastic deformation. When the particle impacts a surface there is some cohesive energy. When a particle is rebounding from a surface there is also some amount of energy from elastic recovery. The rebound energy will be the difference between these two with the elastic recovery energy forcing the particle in a reverse direction and the cohesive energy keeping the particle on the surface. The cohesive energy will increase as the particle and substrate become more bonded, or there is more interaction between the pure metals. When this energy surpasses the rebounding energy the particle cannot break those bonds to leave the surface, resulting in bonding. (**Figure 7**).[48] The oxide layer acts as a barrier, decreasing the cohesive energy and increase the energy available for rebounding. This can explain the large increase in rebound velocities observed in **Figure 21c**. The difference between 10 and 20nm include the appearance of a V_{T2} at 10nm, but when the thickness is increased there seems to be no V_{T2} likely because there is no V_{T1}. With 20nm of oxide added to the surface, the rebound energy is constantly increasing as the impact velocity increases. This is representative of the particle and substrates inability to effectively absorb the impact energy as it increases. At 10nm, it is seen to be able to reach a rebound energy threshold from 400 to 650m/s, but it is still much higher than with no additional oxide. The changes in the critical velocity as a function of thickness and the changes in the absorbed energies are shown in **Figure 22**. The critical velocity also changed as expected, showing a higher impact velocity being required for thicker surface oxide layer. More rebound energy must be absorbed for there to be bonding with thicker oxide layers as well, indicating a larger cohesive force being required to overcome these large rebound forces opposing bonding.

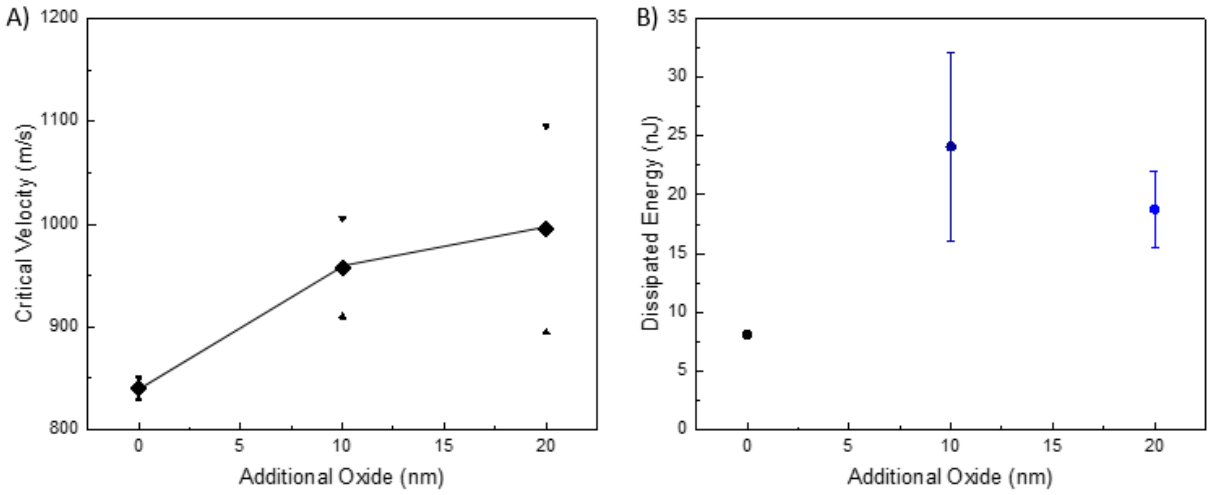

Figure 22: A) The normalized critical velocity as a function of surface oxide thickness. B) the dissipated energy as a function of surface oxide thickness. The dissipated energy was calculated for at particle of diameter 20μm with the rebound energy observed just prior to the critical velocity.

In order to understand the effects, the increased oxide layer had acting as a bonding barrier, cross sectional images of bonded particles to a surface with an additional 20nm of oxide were taken. The cross sectioning is done using xenon plasma focused ion beam milling and shown in **Figure 23**. Two particles that have bonded to the surface are cross sectioned. Similar grain boundary textures resulting from the internal viscous flow of material can be seen to those of particles bonded with no additional oxide (**Figure 11**).[52] The grain boundaries in both the particle and substrate have taken on a more compacted and fluid like appearance, indicating viscous fluid-like flow of material during bonding.

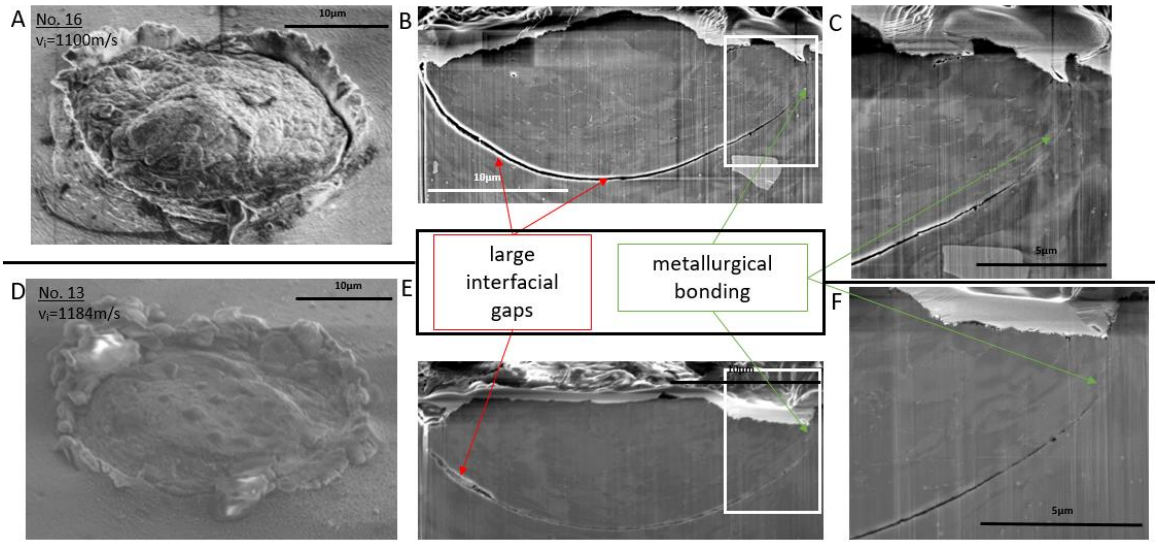

Figure 23: A) off normal SEM image of bonded particle (V_i=1100m/s) to a AA6061 surface with an additional 20nm oxide surface layer. B) SEM image of the cross section of the particle, performed with FIB milling. C) Maginified region of the interface between the paricle and the substrate, highlighing an area of bonding. D-F) Same imaging analysis on a bonded particle with V_i=1184m/s.

The precence of large interfacial gaps, not seen in paticles bonded with no additional substrate, is the most important indication of the effect of the oxide layer. The cross sectional images show that the thicker oxide will in fact act as a barrier when bonding. Furthermore, there will be an attempt to debond the paticle from the substrate, represented by the large and wide gap between the paricle and substrate. This supports the conclusion derived from simulation by Yildirim *et al.*[48] **Figure 23c,f** also shows region where meturallerical bonding was successful by removing the oxide and exposing the pure surfaces. These regions of bonding can be found toward the edges of the intercaial region at the surface. This supports the bonding theory widely accepted. The oxide is more easily moved out of the way to expose the pure metals for bonding from the regions closest to the edge. The material is pushed into the jet formed by this highly deformed material, also present in **Figrue 23a,d**. These cross sectional images represent

the current bonding theary presented in **Figure 3** well by highlighting regions of bonding and regions of the oxide layer acting as a barrier.

Discussion

From the results presented in the previous sections, there were several expected and unexpected phenomena recorded in the experimental data. Expected results were discussed formerly. These are results that were predicted or supported by the data presented in the literature. These included a lower rebound speed for high temperature collisions against a hard substrate (**Figure 15e**), a critical velocity decrease with increasing temperature (**Figure 20a**), and increased critical velocity with increased surface oxide film thickness (**Figure 22a**) to highlight a few. This section will be a discussion of the various results that were not expected from these experiments and will present a potential explanation for them, connecting the high temperature experiments to the additional oxide thickness experimental results.

The results that were not predicted include, first, the higher rebound velocities of collisions of particle on AA6061 observed at elevated temperatures (**Figure 20e**). Second, the small increase in critical velocity from room temperature to 100℃, when the critical velocity was expected to linearly decrease, which was the case as the temperature increased to 300℃ (**Figure 20a**), however at all elevated temperatuers the critical velocity was higher than expected from **Equation 5**. Lastly, was the increase in bonding energy or cohesive force required at elevated temperatures, which is a result of the higher rebound speeds oberved (**Figure 20b**).

It is widely accepted that increaseing the temperature of a ductile metal will result in the theraml softening of the material. This is supported through the literature and

shown in **Figure 8**.[64] Temperature is also known to have another effect on metals, accelerating an oxidation rate. As discussed alumium exposed to increased temperature will see an increase in the oxide thickness at the surface of both a substrate and a particle.[70, 74] It was concluded that for an aluminuim particle of 10-30μm in diameters, the oxide percentage would not see an increase until the temperarure reached over 400℃,[74] which is higher than the experiments performed here. Furhtermore, it is important to note that the AA601 micro particles were annealed at 250℃ for one hour during synthesis. However, for an alumium surface exposed to elevated temperatue, the oxide surface layer thickness will increase by a few nanometers. This incease showed to be independent of time and proportional to increasing temperature.[70] Although AA6061 is heat treated, during the polishing process of the substrate for the experiments any surface oxide was removed and a new surface was allowed to oxidize, first at room temperarure until the experiments were performed and the substrate was exposed to a higher temperature. The experimental results show that there was likely a growth in the oxide layer thickness on the high temperature expirments.

The effect of increasing the oxide thickness on the dynamic response was proven experimentally in **Figure 21-23,** confiming previously theorized and simulated phenomena. When observing and compairing the results of the intentionally increased oxide thickness, there is observabel increases in the rebound and critical velocities, unexpectadly observed in the trends of the high temperature experiments. Increased oxide thickness is a logical explaination for these unanticipated dynamic responces. However, there are predicted responses in the high temperature collisions as well. First, there is a decrease in rebound speed from 200 to 300℃, though still higher than rebound speeds

observed at room temperarture. This corresponds well with the dramatic decrease in material strength from 200 to 300℃, which had an obervable offect on the sapphire collisions (**Figure 15e**). Second, there is a decrease in critical velocity at temperatues past 100℃. This also corresponds well with the decreases in material strength of AA6061 presented in **Figure 8.**

In order to address the thermally increased oxide thickness, the experiments were repeated at 300℃, however a new alumium subtrate was used each time. This was done to see if the oxide growth could be minumized by less time exposed to the high temperatures. Appendix A, shows a graph of the experiments done on a fresh surface with less than one hour exposed to 300℃ and the other experimental results, where the subtrate was not fresh and the exposer time was not considered. The results appear to have a good match, indicating that the experiments do not show a relationship to the time exposed to heat. If the effects on the dynamic response are caused by thermally grown oxide layer, this shows that the oxide growth that takes place must happen rapidly, and reach some saturated point, where the thickness does not continue to increase. This can be concluded because the experiment shows no relation to the time exposed to heat.

The experimental data presetented shows results that were not predicted by the literature. The reason for this is that the effect of the oxide thickness on the dynamic response of HSR collisions was much greater than previously thought. This is highlighed by experiments performed with thicker oxide layers intentially grown on the impact surface. The effect on the collision dynamics was vast (**Figure 21**). When collisions were performed at elevated tempertures, there was an increase in the oxide layer thickness brought on by the high temperature environment. However, the effect of a thicker oxide

layer is in direct competition with the thermal softening present at elevated temperatures. The thicker oxide layer will act as a bonding barrier and cause increases in the rebound speed and decrases in the cohesive energy. The increased thermal softening will cause greater plastic deformtion resulting in decreased rebound speeds and increased cohesive energy by allowing easier flow of the oxide barrier, incrased material ejection, and exposure of pure metal surfaces. At tempertures below 300℃ for impacts with an AA6061 substrate the increased oxide thickness seems to dominate. Only the decrease in cricial velocity at 200℃ expressed a stronger thermal softening effect, showing that perhaps temperature has a greater effect on the critical velocity than the oxide thickness, or that the increase in oxide thickness nominal between 100 and 200℃.[74] Once past 300℃, where there is the most dramatic decrease in AA6061 strength, thermal softening becoms dominant over the increased oxide thickness, resulting in a lower critical velocity and rebound velocity. This data shows that increases in temperature will effect the material in a HSR impact but not in as linear fashion as predicted.[83] Futhermore, the effect of the oxide thickness needs to be strongly considered when developing CS models. This data shows that the dynamic response of the HSR impacts are sensative to the oxide layer thickness, which can be effected by elevated temperatures.

CHAPTER 5

CONCLUSION

CS is a field that has been growing for many years, with numerous industries and disciplines involved with the advancement of this promising method of addictive manufacturing. Due to the extreme nature of the plastic deformation fundamental to CS, it has proven to be challenging to observe and understand. There have been several hypotheses as to the underlying material science governing the bonding mechanisms required for the successful implementation of CS. These include mechanical interlocking of the deposited particle layers, adiabatic shear instabilities resulting in both the cracking and extrusion of the surface oxide leading to exposure of pure metals for cohesive bonding, the extreme interfacial temperature rise leading to local melting, and shock wave induced material jet formation.

Recent work by Xie *et al.* uses the α-LIPIT to simulate the CS process in a far more controlled environment. The α-LIPIT is uniquely advantageous because it allows for single micro particles to be accelerated to velocities similar to those required for CS deposition. In this test, the impact and post collision parameters are able to be observed and accurately measured. Xie *et al.* performs tests on AA6061 micro particles at various speeds and diameters impacting both sapphire and polished AA6061 substrates at room temperature. Through these impact tests, evidence of bonding hypotheses are provided, such as the presence of local melting and cohesive bonding. Another important result from the α-LIPIT data from AA6061-sapphire impacts is the calibration and validation of the most recent CS simulation, further improving its accuracy by directly comparing the simulated outcomes to those experimentally derived and adjusting model variables to

match the two. This method vastly improves the CS simulation accuracy and reliability of any conclusions drawn from it. This initial demonstration of using the α-LIPIT to mimic the CS process while allowing for accurate characterization of the collision proved to be successful. The small variations in diameter prove to not have a measured impact on the dynamic response in these experiments and is the reason that they are ignored during this work. However, it is clear that other dynamic variables present in CS including temperature, impact angle, and oxide thickness should be studied which is the goal of the work presented above.

In order to further understand the complex CS process, impact parameters are varied through additions to the α-LIPIT system. Elevating the temperature of the collision environment is made possible through the addition of an insulated heating chamber, which allows for the α-LIPIT system to function normally while in use. Initial results are derived using this high-strain-rate impact test to observe the dependence of the CS process on the temperature. When impacting sapphire, the elastic rebound velocity is not effected until a temperature of 300 ℃ is reached. This leads to the hypothesis that, during high strain rate impacts on ideal-hard surfaces, thermal softening does not have a large effect on the particles' deformation until the temperature surpasses 300℃, which corresponds to a dramatic drop in material strength. This data will add to the calibration of the most current CS simulation.

It is discovered, through observation of the collisions of AA6061 micro particles to a polished AA6061 substrate, that the critical velocity is lowered at elevated temperatures, which was predicted. However, the critical velocity did not lower until the temperature exceeded 100℃. Furthermore, the rebound velocity actually increased rather

than decreasing for temperatures less than 300℃, which remained higher than room temperature experiments as well. These unexpected phenomena are attributed in this work to the increases in oxide layer thickness with increasing temperature. In order to understand the effect the thickness of the oxide layer has on the dynamic response of CS particles, α-LIPIT was performed on substrates with intentionally increased oxide layer thicknesses. It is discovered that there is an increase in the rebound and critical velocity when the oxide layer thickness increases. This is to be expected based on the previously theorized bonding phenomenon and the surface oxides role as a bonding barrier. Study of the cross sectional area of bonded particles show that, even at high impact velocities, there are large amounts of unbonded areas, which is likely a result of the collisions inability to remove the thicker oxide layer.

The dynamic response of the α-LIPIT experiments with increased oxide thickness support the hypothesis that the oxide thickness is the cause of unpredicted dynamic responses in the elevated temperature experiments. This indicates that the oxide thickness must have a larger effect on the dynamic response of CS particles than previously thought. The effect of increased temperature must be connected to the effect of increased surface oxide thickness when attempting to understand the real phenomena in this extreme collision event because even slight increases in the oxide thickness have an impact on the dynamic response and the bonding capabilities of particles. The experimental data presented here can be used to bolster current simulation techniques in order to gain further understanding of the widely unknown and contested governing material science in cold spray.

APPENDIX A

FIGURES

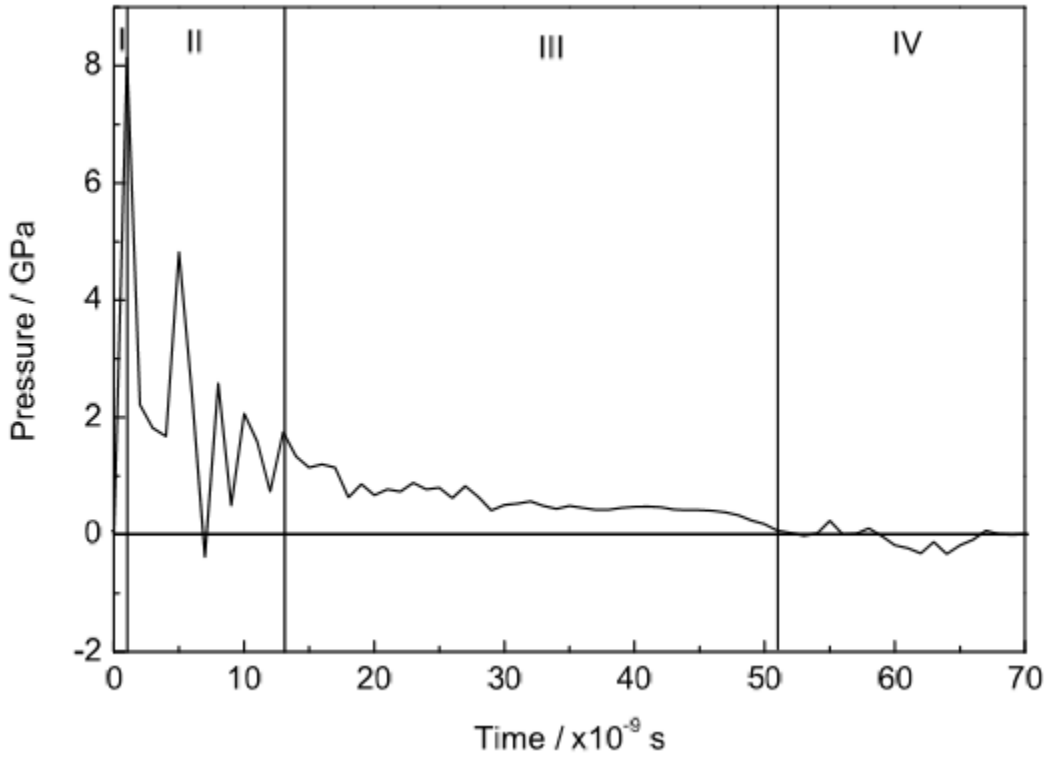

Figure A1: Pressure fluctuations as a function of time for simulated copper particles impacting a copper substrate at a velocity of 600 m/s. The four stages discussed are defined.[33]

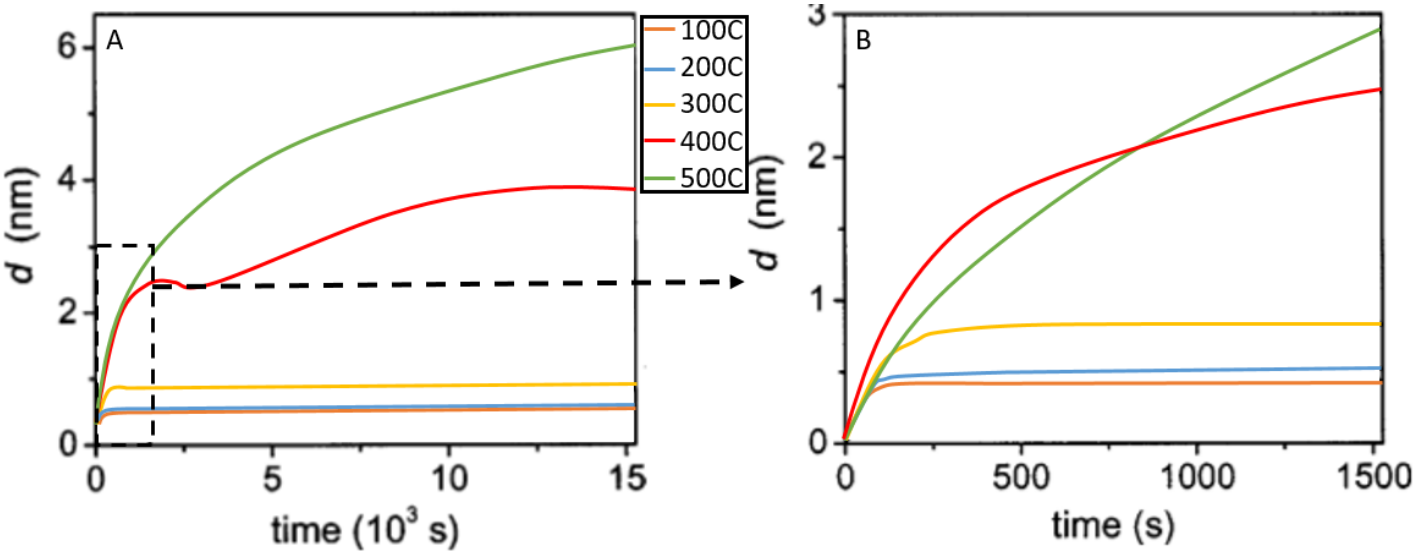

Figure A2: Oxide film thickness (d) grown on fresh pure aluminum as a function of time at different temperatures in a low oxygen environment (10^{-4}Pa). B. an inset of the lower region of A.[70]

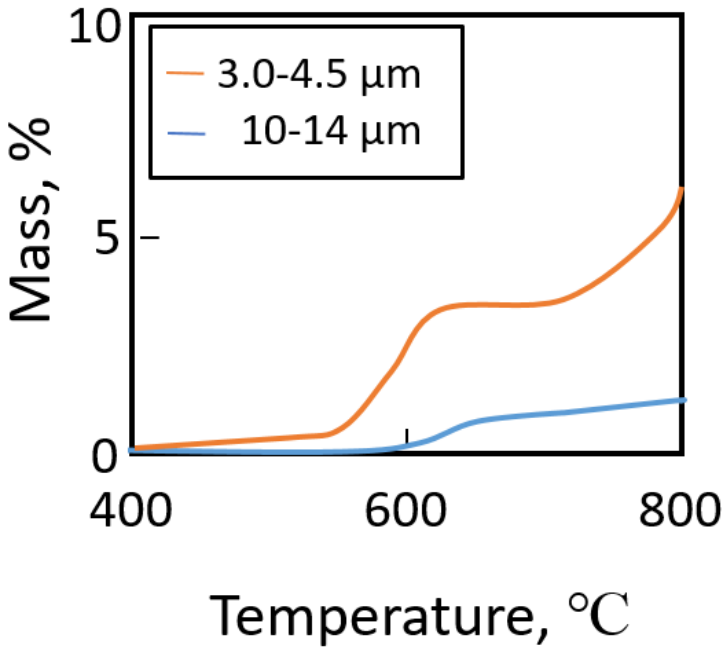

Figure A3: Percentage of aluminum oxide in aluminum particles of two different diameters as a function of increasing temperature.[74]

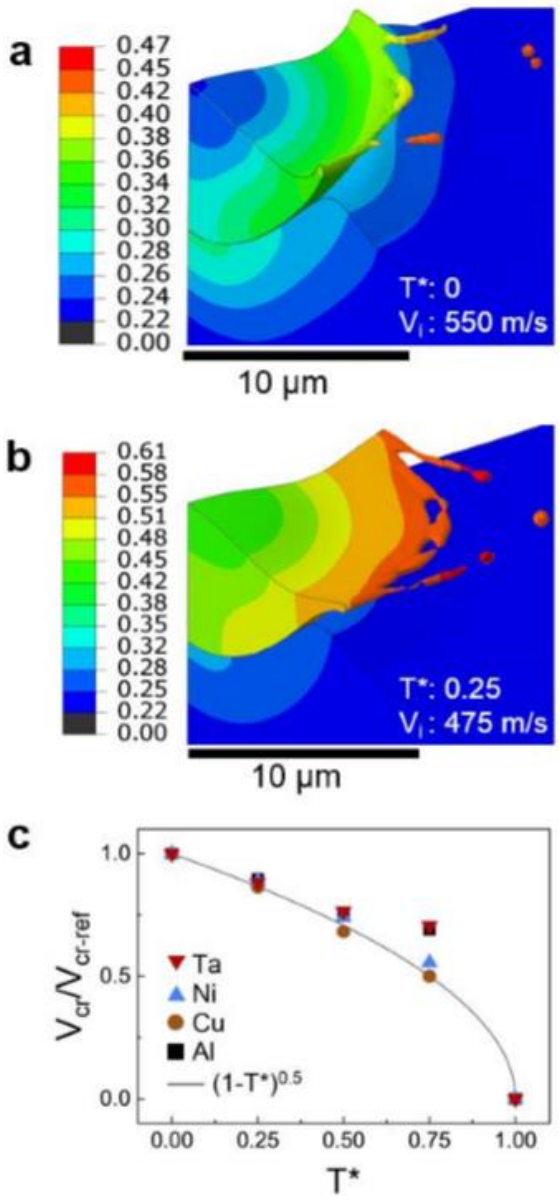

Figure A4: Deformation of 10μm diameter copper particles impacting a copper substrate at A) 298K and a critical velocity of 550m/s and B) 563K and a critical velocity of 475m/s. Particles at higher temperatures have more deformation and less penetration. C) with increasing initial particle temperature the critical velocity decreases in a manner that can be reasonably fitted with a square root relation that disappears at the melting point, Equation 4.[83]

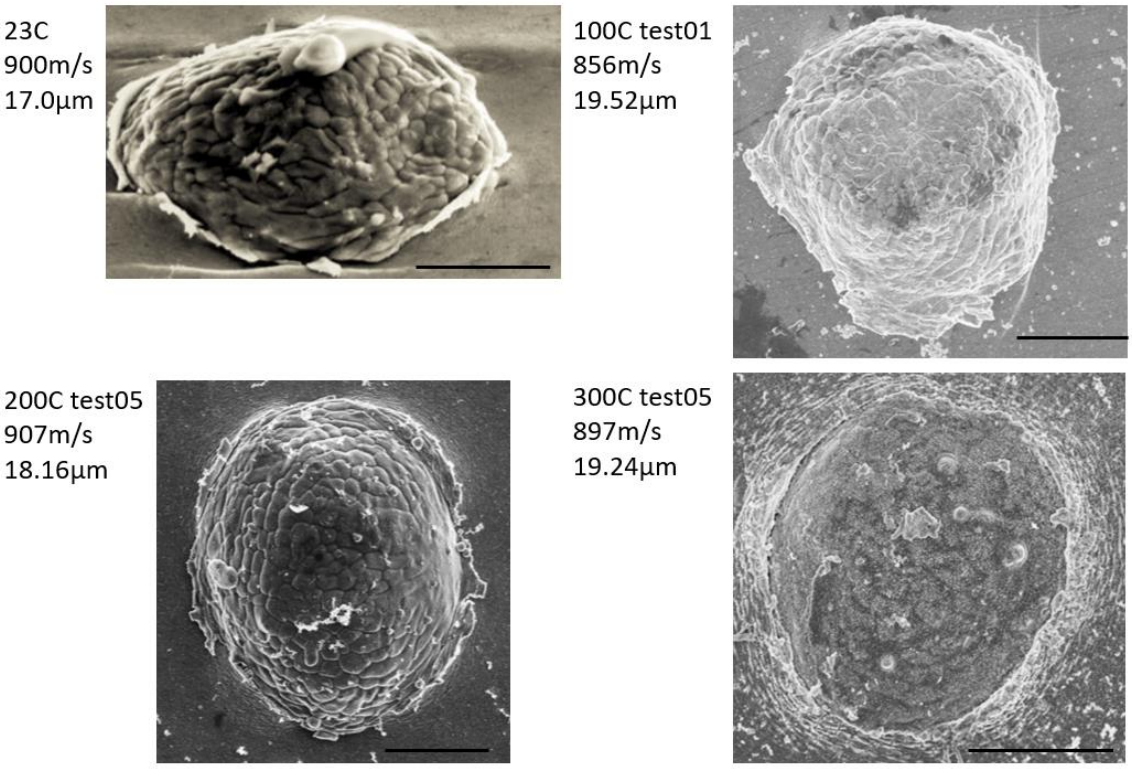

Figure A5: SEM images of bonded AA6061 particles to an AA6061 substrate a varying temperatures. The particles all show the presence of the jet region on the outer edge.

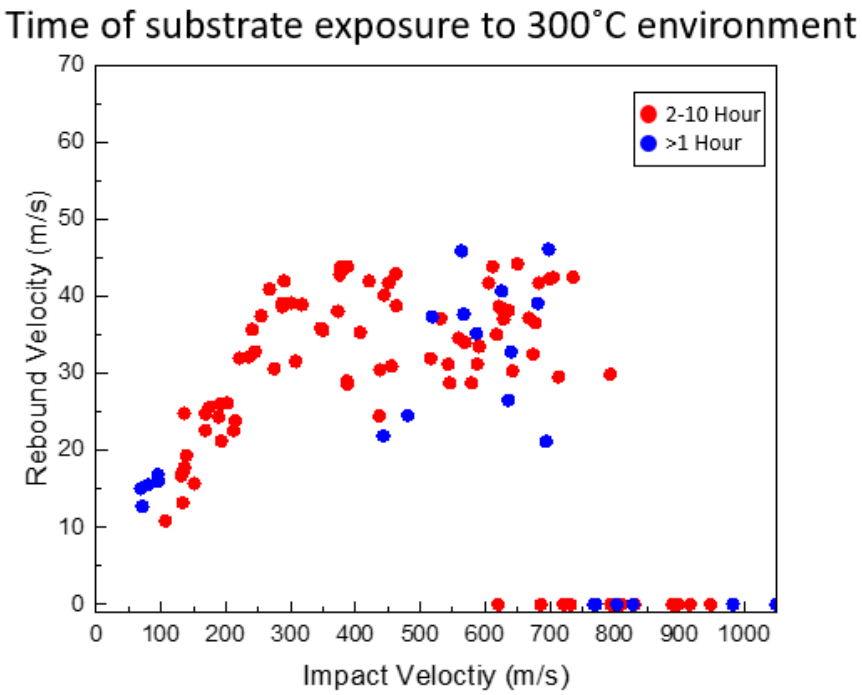

Figure A6: Plot of the rebound velocities as a function of impact velocity for particles impacting an AA6061 substrate at 300°C. In red, are particles without consideration of the time the substrate was exposed to the high temperature, it is predicted that this time is between 2-10 hours. In blue, is experiments performed on a substrate that was exposed to the heat for less than 1 hour.

APPENDIX B

TABLES

Table B1: Values of components and common material properties of AA6061.[63]

Properties	Parameter	AA6061
General	Density (g/cc)	2.7
	Brinell Hardness	95
	Ultimate Tensile Strength (MPa)	310
	Yield Strength (MPa)	276
	Modulus of Elasticity (GPa)	68.9
	Poisson's Ratio	0.33
	Shear Modulus (GPa)	26
	Shear Strength (MPa)	207
Thermal	Specific Heat (J/g C)	896
	Melting Temperature (C)	582-651
	Thermal Conductivity (W/m K)	167
Component Elements (%)	Aluminum	95.8-98.6
	Chromium	0.04-0.35
	Copper	0.15-0.4
	Iron	0-0.7
	Magnesium	0.8-1.2
	Manganese	0-0.15
	Silicon	0.4-0.8
	Titanium	0-0.15
	Zinc	0-0.25
	Other	0-0.15

Table B2: Material properties (at 293K) used in the model and optimized equation variables.[52]

Properties	Parameter	AA6061	Sapphire
General	Density (kg/m²)	2,700	3,980
	Specific heat (J/kg K)	1,009	755
	Thermal conductivity (W/m K)	145	33
	Thermal expansion (10^{-6}/K)	22.3	4.6
	Melting temperature (K)	925	-
	Inelastic heat fraction	0.9	-
	Maximum tensile stress (MPa)	300	-
Elastic	Elastic modulus (GPa)	69.11	416
	Poison's ratio	0.331	0.231
Material failure	Failure strain	3	-
Cohesion	Cohesive bond energy (J/m²)	0.5	-
Plastic (Johnson-Cook plasticity model)	A	270	-
	B	154.3	-
	n	0.239	-
	C_1	2×10^{-3}	-
	C_2	29×10^{-3}	-
	m (temperature exponent)	1.42	-
	$\dot{\varepsilon}_C$	597.2	-
	Reference strain rate (s^{-1})	1	-
	Reference temperature (K)	293	-

Table B3: Material data used in simulations.[83]

	Cu	Ni	Al	Ta
Density (kg/m^3)	8960	8908	2700	16690
Specific heat (J/kg K)	384.6	444.2	896.9	140.2
Melting temperature (K)	1357	1728	933	3290
Heat of Fusion (kJ/kg)	208.7	297.8	396.9	202.1
Conductivity (W/m K)	401	90.9	237	57.5
Shear Modulus (GPa)	48	76	26	69
Poisson's ratio	0.34	0.31	0.35	0.34
Bulk Modulus (GPa)	140	180	76	200
C_0 (m/s)	3952.8	4495.2	5305.5	3461.7
s	1.49	1.44	1.339	1.2
Γ_0	2.01	1.83	2.17	1.61
A (MPa)	90	163	148.4	684.5
B (MPa)	292	648	345.5	205.3
n	0.31	0.33	0.183	0.78
C	0.025	0.006	0.001	0.043
m	1.09	1.44	0.895	0.344
$\dot{\varepsilon}_0$ (s^{-1})	1	1	1	3500
T_{ref} (K)	298	298	293	298

REFERENCES

[1] A. M. Ang, N. Sanpo, M. I. Sesso and C. C. Berndt, *Journal of Thermal Spray Technology*, vol. 22, no. 7, pp. 1170-1183, 2013.

[2] R. Thevamaran, O. Lawal, S. Yazdi, S. J. Jeon, J. H. Lee and E. L. Thomas, "Dynamic creation and evolution of gradient nanostructure in single-crystal metallic microcubes," *Science,* vol. 354, no. 6310, pp. 312-316, 2016.

[3] T. H. Fang, W. L. Li, N. R. Tao and K. Lu, "Revealing extraordinary intrinsic tensile plasticity in gradient nano-grained copper," *Science,* vol. 331, no. 6024, pp. 1587-90, 2011.

[4] K. Lu, "Making strong nanomaterials ductile with gradients," *Science,* vol. 345, no. 6203, pp. 1455-56, 2014.

[5] A. Papyrin, V. Kosarev, S. Klinkov, A. Alkhimov and V. Fomin, Cold Spray Technology, Amsterdam: Elsevier Science, 2007.

[6] A. P. Alkhmov, A. N. Papyrin, V. F. Dosarev, N. I. Nestorovich and M. M. Shuspanov, "Gas dynamic spraying method for applying a coating," *US Patent,* vol. 5, no. 302, p. 414, 1994.

[7] A. O. Tokarev, "Structure of aluminum powder coatings prepared by cold gas dynamic spraying," *Material Science and Heat Treatment,* vol. 35, no. 7, pp. 136-139, 1996.

[8] E. Irisson, J. G. Legoux, A. N. Ryabinin, B. Jodoinm and J. Moreau, "Review on cold spray process and Technology," *Thermal Spray Technology,* vol. 17, no. 4, pp. 495-516, 2008.

[9] V. K. Champagne, The cold spray materials deposition process, Woodhead Publishing, 2007.

[10] Q. Wang and M. Zhang, "Review on recent research and development of cold spray technologies," *Key Engineering Materials,* vol. 533, pp. 1-52, 2013.

[11] A. Moridi, S. M. Hassani-Gangaraj, M. Guagliano and M. Dao, "Cold spray coating: review of material systems and future perpectives," *Surface Engineering,* vol. 36, no. 6, pp. 369-395, 2014.

[12] T. Schmidt, H. Assadi and F. Gartner, "From particle acceleration to impact and bonding in cold spraying," *Thermal Spray Technology,* vol. 18, pp. 794-808, 2009.

[13] T. Stoltenhoff, H. Kreye and H. J. Richter, "An analysis of the cold spray process and its coatings," *Thermal Spray Technology,* vol. 11, no. 4, pp. 542-550, 2002.

[14] R. C. McCune, A. N. Papyrin, J. N. Hall, W. L. Riggs and P. H. Zajchowski, an exploration of the cold-gas-dynamics spray method for several materials systems: Advances in thermal spray science and technology, Materials Park: ASM International, 1995.

[15] M. Grujicic, J. R. Saylor, D. E. Beasley, W. S. DeRosset and D. Helfritch, "Computational Analysis of thInterfacial bonding between feed-powder particles and the substrate in the cold-gas dynamic-spray process," *Applied Surface Science,* vol. 219, no. 3, pp. 211-227, 2003.

[16] T. Schmidt, F. Gartner and H. Kreye, "High strain rate deformation phenomena in explosive powder compaction and cold gas spraying," in *Proceedings of the ITSC*, Materials Park, ASM International, 2003, pp. 9-17.

[17] S. Klinkov, V. Kosarev and M. Rein, "Cold spray deposition: Significance of particle impact phenomena," *Aerospace Science and Technology,* no. 9, pp. 582-591, 2005.

[18] H. Assadi, H. Kreye, F. Gartner and T. Klassen, "Cold spraying- A materials perspective," *Acta Materialia,* vol. 116, pp. 382-407, 2016.

[19] S. Grigoriev, A. Okunkova, A. Sova, P. Bertrand and I. Smurov, "Cold spraying: from process fundamentals towards advanced applications," *Surface Coating Technologies,* vol. 268, pp. 77-84, 2015.

[20] T. G. F. A. H. K. H. Schmidt, "Development of a Generalized Parameter Window for Cold Spray Deposition," *Acta Materialia,* vol. 54, no. 3, pp. 729-742, 2006.

[21] M. Z. C. L. D. W. S. H. D. Grujicic, "Adiabatic Shear Instability Based Mechanism for Particles/Substrate Bonding in the ColdGas Dynamic-Spray Process," *Materials and Design,* vol. 25, no. 8, pp. 681-688, 2004.

[22] T. M. D. G. S. P. H. D. Hussain, "Bonding Mechanisms in Cold Spraying: The Contributions of Metallurgical and Mechanical Components," *Thermal Spray Technology,* vol. 18, no. 3, pp. 364-379, 2009.

[23] G. X. Y. K. S. K. K. L. C. Bae, "General Aspects of Interface Bonding in Kinetic Sprayed Coatings," *Acta Materialia,* vol. 56, no. 17, pp. 4858-68, 2008.

[24] I. M. V. Manna, *Material Science Letters,* vol. 12, pp. 920-922, 1993.

[25] M. K. S. Watanabe, "High-speed deformation and collision behavior of pure aluminum plates in magnetic pulse welding," *Material Transactions,* vol. 50, pp. 2035-42, 2009.

[26] A. K. V. K. S. A. A. Papyrin, "On the interaction of high speed particles with a substrate under the cold spray," *International Thermal Spray Conference,* 2002.

[27] S. W. T. Schoenfeld, "A failure criterion based on material instability," *Solids Structure,* vol. 40, pp. 3031-37, 2003.

[28] H. G. F. S. T. &. K. H. Assadi, "Bonding mechanism in cold gas spraying.," *Acta Materialia,* vol. 51, pp. 4379-94, 2003.

[29] W.-Y. L. H. L. C.-J. L. G. C. C. a. W. X. Li, "On High Velocity Impact of Micro-Sized Metallic Particles in Cold Spraying," *Applied Surface Science,* vol. 253, no. 5, pp. 2852-62, 2006.

[30] W.-Y. L. H. L. C.-J. B. H.-S. C. C. Li, "Numerical Simulation of Deformation Behavior of Al Particles Impacting on Al Substrate and Effect of Surface Oxide Films on Interfacial Bonding in Cold Spraying," *Applied Surface Science,* vol. 253, no. 11, pp. 5084-91, 2007.

[31] A. G. F. M. T. S. M. A. H. K. S. K. T. List, "Cold spraying of amorphous Cu50Zr50 alloys," *Thermal Spray Technology,* vol. 24, pp. 108-118, 2014.

[32] W. L. C. Y. G. Li, "Effect of impact-induced melting on interface microstructure and bonding of cold-sprayed zinc coating," *Applied Surface Science,* vol. 257, no. 5, pp. 1516-23, 2010.

[33] X. Zhoe, X. Wu, J. Wang and J. Zhang, "Numerical Investigation of the rebound and the deposition behavior of particles during cold spraying," *ACTA Metallurgical Sinica,* vol. 24, no. 1, pp. 43-53, 2011.

[34] W.-Y. L. H. L. C.-J. B. H.-S. a. C. C. Li, "Numerical Simulation of Deformation Behavior of Al Particles Impacting on Al Substrate and Effect of Surface Oxide Films on Interfacial Bonding in Cold Spraying," *Applied Surface Science,* vol. 253, no. 11, pp. 5084-91, 2007.

[35] G. Bae, S. Kumar, S. Yoon, K. Kang, H. Na, H. Kim and C. Lee, "Bonding features and associated mechanisms in kinetic sprayed titanium coatings," *Acta Materialia,* vol. 57, pp. 5654-66, 2009.

[36] R. C. S. M. F. G. D. L. N. R. A. J. X. S. S. Dykhuizen, "Impact of High Velocity Cold Spray Particles," *Thermal Spray Technology,* vol. 8, no. 4, pp. 559-564, 1999.

[37] K. W. M. K. S. G. Y. S. T. G. F. Yokoyama, "Simulation of Solid Particle Impact Behavior for Spray Processes," *Material Transaction,* vol. 47, no. 7, pp. 1697-1702, 2006.

[38] W. Li, X. Zhang, C. Guo, H. Li, H. Liao and C. Coddet, "Study on impact fusion at particle interfaces and its effect on coating microstructure in cold spraying," *Applied Surface Science,* vol. 254, pp. 517-526, 2007.

[39] S. B. G. a. L. C. Kumar, "Deposition Characteristics of Copper Particles on Roughened Substrates Through Kinetic Spraying," *Applied Surface Science,* vol. 255, no. 6, pp. 3472-79, 2009.

[40] W.-Y. Y. S. a. W. X.-F. Li, "Numerical Investigations of the Effect of Oblique Impact on Particle Deformation in Cold Spraying by the SPH Method," *Applied Surface Science,* vol. 256, no. 12, pp. 3725-34, 2010.

[41] B. M. S. a. G. A. Yildirim, "Modeling of High Velocity Impact of Spherical Particles," *Wear,* vol. 270, no. 9-10, pp. 703-713, 2011.

[42] S. W. X.-F. L. W. Y. a. J. H.-E. Yin, "Effect of Substrate Hardness on the Deformation Behavior of Subsequently Incident Particles in Cold Spraying," *Applied Surface Science,* vol. 257, no. 17, pp. 7560-65, 2011.

[43] S. W. X.-F. X. B.-P. a. L. W.-Y. Yin, "Examination on the Calculation Method for Modeling the Multi-Particle Impact Process in Cold Spraying," *Thermal Spray Technology,* vol. 19, no. 5, pp. 1032-41, 2010.

[44] X.-L. W. X.-K. G. H.-H. W. J.-G. a. Z. J.-S. Zhou, "Deposition Behavior of Multi-Particle Impact in Cold Spraying Process," *Mineral and Materallurgical Materials,* vol. 17, no. 5, pp. 635-640, 2010.

[45] C.-J. L. W.-Y. a. L. H. Li, "Examination of the Critical Velocity for Deposition of Particles in Cold Spraying," *Thermal Spray Technology,* vol. 15, no. 2, pp. 212-222, 2006.

[46] W.-Y. L. H. L. C.-J. L. G. C. C. a. W. X. Li, "On High Velocity Impact of Micro-Sized Metallic Particles in Cold Spraying," *Applied Surface Science,* vol. 253, no. 5, pp. 2852-62, 2006.

[47] J. K. H. W. M. Y. K. a. K. S. Kawakita, "Warm Spraying: An Improved Spray Process to Deposit Novel Coatings," *Surface Coating Technology,* vol. 202, no. 18, pp. 4369-73, 2008.

[48] B. H. F. T. A. A. G. a. S. M. Yildirim, "A Numerical Investigation Into Cold Spray Bonding Processes," *Jounal of Tribology,* vol. 137, 2015.

[49] A. a. R. R. Seagraves, "Advances in Cohesive Zone Modeling of Dynamic Fracture," in *Dynamic Failure of Materials and Structures*, Berlin, Springer, 2010, pp. 349-405.

[50] J. R. Rice, "Mathematical Analysis in the Mechanics of Fracture," in *Fracture: An Advanced Treatise, Vol 2*, New York, Academic, 1968, pp. 191-311.

[51] G. R. a. C. W. H. Johnson, "A Constitutive Model and Data for Metals Subjected to Large Strains, High Strain Rates and High Temperature," in *Proceedings of Seventh International Symposium on Ballistics*, Netherlands, The Hague, 1983, pp. 541-547.

[52] W. Xie, A. Alizadeh-Dehkharghani, Q. Chen, V. K. Champagne, X. Wang, A. T. Nardi, S. Kooi, S. Muftu and J. H. Lee, "Dynamics and extream plasticity of metallic microparticles in supersonic collisions," *Scientific Reports,* vol. 5073, 2017.

[53] V. K. Champagne and D. J. Helfritch, "Mainstreaming cold spray-push for applications," *Surface Engineering,* vol. 30, pp. 396-403, 2014.

[54] X. Wu, X. Zhoe, H. Cui, X. Zheng and J. Zhang, *Thermal Spray,* vol. 5, no. 21, pp. 792-799, 2012.

[55] M. Rokni, C. Widener and V. Champagne, "Microstructural stability of ultrafine grained cold sprayed 6061 aluminum alloy," *Applied Surface Science,* vol. 290, pp. 482-489, 2014.

[56] M. Rokni, C. Widener, G. Crawford and M. West, "An investigation into microstructure and mechanical properties of cold sprayed 7075 Al deposition," *Material Science Engineering,* vol. 625, pp. 19-27, 2015.

[57] P. Vo, E. Irissou, J. Legoux and S. Yue, "Mechanical and microstructural characterization of cold-sprayed Ti-6Al-4V after heat treatment," *Thermal Spray Technology,* vol. 22, pp. 954-964, 2013.

[58] X. Meng, J. Zhang, W. Han, J. Zhao and J. Liang, "Influence of annealing treatment on the microstructure and mechanical performance of cold sprayed 304 stainless steel coating," *Applied Surface Science,* vol. 258, pp. 700-704, 2011.

[59] B. Mangour, P. Vo, R. Mongrain, E. Irissou and S. Yue, "Effect of heat treatment on the microstructure and mechanical properties ofstainless steel 316L coatingsproduced by cold spray for biomedical applications," *Thermal Spray Technology,* vol. 23, pp. 641-652, 2014.

[60] M. W. C. O. O. C. G. Rokin, "Microstructure and mechanical properties of cold sprayed 6061 Al in As-sprayed and heat treated condition," *Surface Coatings Technology,* vol. 309, pp. 641-650, 2017.

[61] M. Rokni, C. Widener and V. Champagne, "Microstructural evolution of 6061 aluminum gas-atomized powder and high-pressure cold-sprayed deposition," *Thermal Spray Technology,* vol. 23, pp. 514-524, 2014.

[62] B. &. B. A. S. Banerjee, "An extended mechanical threshold stress plasticity model: Modeling 6061-t6 aluminum alloy," *Mechanical Material Structures,* vol. 3, pp. 391-424, 2008.

[63] A. International, "Properties and selection: Nonferrous alloys and special purpose materials," *Metals Hanbook,* p. 10, 1990.

[64] P. Summers, Y. Xhen, C. Rippe, B. Allen, A. Mouritz, S. Case and B. Lattimer, "Overview of aluminum alloy mechanical properties during and after fires," *Fire Science Review,* pp. 2-26, 2015.

[65] P. Summers, S. Case and B. Lattimer, "Resicual mechanical properties of aluminum alloys after fire," *Engineering Structures,* pp. 49-61, 2014.

[66] M. Fukumoto, H. Wada, K. Tanabe, M. Yamada, E. Yarmaguchi, A. Niwa, M. Sugimoto and M. Izawa, "Effects of substrate temperautre on deposition behavior of copper particles on substrate surfaces in cols spray process," *Thermal Spray Technology,* vol. 16, pp. 643-650, 2007.

[67] Y. Watanabe, C. Yoshida, k. Atsumi, M. Yamada and M. Fukumoto, "Influence of substrate temperature on adhesion strength of cold-sprayed coatings," *Thermal Spray Technology,* vol. 24, pp. 86-91, 2015.

[68] X. K. Suo, M. Yu, W. Y. Li, M. P. Planche and H. I. Liao, "Effect of substrate preheating on bonding strength of cold sprayed Mg coatings," *Thermal Spray Technology,* vol. 21, pp. 1091-98, 2012.

[69] Z. V. V. M. A. H. G. F. K. T. Ababgol, "Influence of thermal properties and temperature of substrate on the quality of cold sprayed deposits," *Acta Materialia,* vol. 127, pp. 287-301, 2017.

[70] L. Jeurgens, W. Sloof, F. Tichelaar and E. Mittemeijer, "Growth kinetics and mechanicms of aluminum oxide films formed by thermal oxidation of alumium," *Journal of Applied Physics,* p. 1649, 2002.

[71] K. Y. S. J. Y. a. L. C. Kang, "Oxidation Dependency of Critical Velocity for Aluminum Feedstock Deposition in Kinetic Spraying Process," *Material Science Engineering,* vol. 486, no. 1-2, pp. 300-307, 2008.

[72] C. J. W. H. T. Z. Q. Y. G. J. L. W. Y. a. L. H. L. Li, "Influence of Spray Materials and Their Surface Oxidation on the Critical Velocity in Cold Spraying," *Thermal Spray Technology,* vol. 19, no. 1-2, pp. 95-101, 2010.

[73] S. W. X. L. W. L. H. J. H. Yin, "Deformation behavior of the oxide film on the surface of cold sprayed powder particle," *Applied Surface Science,* vol. 259, pp. 294-300, 2012.

[74] M. Trunov, M. Schoenitz, X. Zhu and E. Dreizen, "Effect of polymorphic phase transformations in Al2O3 film on oxidation kinetics of aluminum powders," *Combustion and Flame,* pp. 310-318, 2005.

[75] *Material Property Database ver. 7.99,* JAHM Softeare, Inc., 2016.

[76] E. A. P. D. &. O. D. R. J. de Souza Neto, *Computational methods for plasticity: Theory and applications,* John Wiley & Sons, 2011.

[77] A. L. D. G. L. &. G. M. Manes, "An experimental–numerical investigation on aluminium tubes subjected to ballistic impact with soft core 7.62 ball projectiles," *Thin Wall Structures,* vol. 73, pp. 68-80, 2013.

[78] A. P. L. S. M. &. G. M. Manes, "Analysis of strain rate behavior of an a1 6061 t6 alloy," *Mechanical Behavior of Materials,* vol. 10, pp. 3477-82, 2011.

[79] M. Meyer, "Dynamic Behavior of Materials," *Wiley,* pp. 50-62, 1994.

[80] S. Z. S. G. A. &. A. T. Müftü, in *The 38th Annual Meeting of the Adhesion Society,* Savannah, GA, 2015.

[81] T. &. H. K. Uesugi, "First-principles calculation of grain boundary energy and grain boundary excess free volume in aluminum: Role of grain boundary elastic energy," *Material Science,* vol. 46, pp. 4199-4205, 2011.

[82] C.-H. L. S.-Y. H. H.J. Kim, "Fabrication of WC–Co coatings by cold spray deposition," *Surface Coating Technology,* vol. 191, p. 335–340, 2005.

[83] M. Hassani-Gangaraj, D. Veysset, K. Nelson and C. Schuh, "Supersonic impact of metallic microparticles," *Scripta Materialia,* vol. 145, pp. 9-13, 2017.